Economic Geology, v. 109, pp. 1611–1642

Evidence for Syngenetic Precious Metal Enrichment in an Appalachian Volcanogenic Massive Sulfide System: The 1806 Zone, Ming Mine, Newfoundland, Canada[*]

Stefanie M. Brueckner,[1,†] Stephen J. Piercey,[1] Paul J. Sylvester,[1] Stephanie Maloney,[2,**] and Larry Pilgrim[2]

[1] *Department of Earth Sciences, Memorial University of Newfoundland, 300 Prince Philip Drive, St. John's, NL A1B 3X5, Canada*

[2] *Rambler Metals and Mining Canada Limited, Route #418, Ming's Bight Road, NL A0K 3S0, Canada*

Abstract

The Ming deposit, Baie Verte, Newfoundland, Canada, is an Early Ordovician bimodal-mafic, Cu-Au-(Zn-Ag) volcanogenic massive sulfide (VMS) deposit. The deposit consists of a number of ore lenses that are stacked in the uppermost part of the Rambler rhyolite. One of the uppermost lenses, the 1806 zone, is enriched in Au and Ag. The deposit has been affected by Silurian-Devonian greenschist to amphibolite grade metamorphism and polyphase deformation and this has led to debates as to whether the Au-Ag enrichment in the deposit is syngenetic or a product of a later metamorphic and structural overprint.

The 1806 zone consists predominantly of discordant sulfide stringer, stratabound semimassive to massive sulfides and a weakly mineralized silicified cap zone. The ore is largely hosted within the footwall Rambler rhyolite that is strongly altered to quartz-sericite ± green mica with sporadic chlorite-biotite. Base and precious metal zoning is developed from the down-plunge portion (Cu-Au) to the up-plunge portion (Cu-Zn-Au-Ag-Pb) of the 1806 zone. The ore mineralogy and mineral chemistry are complex and are interpreted to be of an intermediate sulfidation type. Pyrite and chalcopyrite are the dominant sulfide species with minor to accessory sphalerite, galena, pyrrhotite, and arsenopyrite. Sulfosalts including Ag-bearing tennantite-tetrahedrite, stannite, boulangerite, and loellingite, and precious metal-rich phases are common throughout the deposit. Precious metals occur as (1) mercurian electrum (7.93–20.57 wt % Hg) and (2) various Ag phases (miargyrite, pyrargyrite, mercurian stephanite, unnamed AgCuFeS phase, Ag-Hg ± Au alloys) that are more abundant in the up-plunge portion of the 1806 zone. Tellurides and bismuthides are present in trace amounts. Oxides (cassiterite and magnetite) are present exclusively in the down-plunge portion of the 1806 zone.

The deposit geometry, metals distribution, complex ore assemblages, abundant sulfosalts, and the significant concentration of the epithermal suite of elements (e.g., Au, Ag, As, Hg, Sb, Bi) in the ore strongly contrast with those of orogenic Au deposits and support a syngenetic or synvolcanic origin for precious metals in the Ming VMS deposit, including a possible magmatic input into the 1806 zone ore-forming system.

Evidence for a late, syndeformation precious metal emplacement via orogenic overprinting is lacking at the 1806 zone and all data point to a syngenetic origin for precious metal enrichment, indicating that Ordovician Appalachian VMS deposits are favorable targets for Au. Nevertheless, Silurian-Devonian metamorphism and deformation have resulted in textural recrystallization and local remobilization of precious metals and the main fabrics largely control the current geometry of the host succession and of the Ming orebody.

Introduction

Precious metal-enriched volcanogenic massive sulfide (VMS) deposits are of growing economic importance in a metal-dependent global economy (Poulsen and Hannington, 1996; Huston, 2000; Dubé et al., 2007a; Mercier-Langevin et al., 2011). These deposits combine geologic and mineralogical characteristics of typical base metal-rich VMS deposits with some specific characteristics of precious metal-rich, high sulfidation epithermal deposits (e.g., Franklin et al., 1981, 2005; Lydon, 1984, 1988; Hannington and Scott, 1989a; Large, 1992; Franklin, 1993, 1996; Ohmoto, 1996; Poulsen and Hannington, 1996; Hannington et al., 1999; Huston, 2000; Poulsen et al., 2000; Dubé et al., 2007a; Galley et al., 2007). In contrast to base metal-only VMS deposits, Au-rich VMS deposits are commonly characterized by one or more of the following features: (1) advanced argillic-style alteration, (2) complex ore mineralogy with abundant arsenopyrite and sulfosalts, (3) enrichments in epithermal suite elements (Ag, As, Au, Bi, Hg, Sb, Te), and (4) an association with andesite-dacite-rhyodacite-rhyolite rocks (Poulsen and Hannington, 1996; Sillitoe et al., 1996; Hannington et al., 1999; Huston, 2000; Poulsen et al., 2000; Dubé et al., 2007a; Mercier-Langevin et al., 2011). Like many ancient VMS deposits, Au-rich VMS deposits are commonly metamorphosed and deformed and often in close proximity to major deformation zones and orogenic Au deposits. This metamorphic overprint and close spatial relationship to orogenic Au deposits often lead to arguments about the origin of precious metal enrichment in these deposits. In the literature, both syngenetic (e.g., Tourigny et al., 1993; Dubé et al., 2007b; Mercier-Langevin et al., 2013) and synorogenic (e.g., Marquis et al., 1990) origins were proposed to explain the precious metal enrichment in VMS deposits. The former, syngenetic concept often involves the contribution of magmatic fluids similar to those in high sulfidation epithermal Au deposits (Sillitoe et al., 1996), mostly based on the presence of the epithermal suite of elements, such as Ag, Au, As, Hg, Sb ± Bi and Te, which commonly enrich such VMS systems. In contrast, the deformed nature of the deposits has led other authors to suggest that precious metals are added subsequent to VMS formation and represent an orogenic precious metal upgrading to mineralization (e.g., Marquis et al., 1990).

[†] Corresponding author: e-mail, s.brueckner@mun.ca

[*] A digital supplement to this paper is available at http://economicgeology.org/ and at http://econgeol.geoscienceworld.org/.

[**] Present address: Vale, Voisey's Bay Mine Site, P.O. Box 7001, Stn. C, Happy Valley-Goose Bay, NL A0P 1C0, Canada.

0361-0128/14/4243/1611-32

Submitted: March 20, 2013
Accepted: November 25, 2013

The Newfoundland Appalachians are a Paleozoic orogenic belt with a diachronous history of magmatism, deformation, and metamorphism, and host both orogenic Au and precious metal-rich VMS deposits. The deposits formed during the various stages of the Appalachian orogenesis during the closure of the Iapetus and Rheic oceans (van Staal, 2007; van Staal and Barr, 2012). The Baie Verte Peninsula, northwest Newfoundland, hosts both precious metal-rich VMS deposits and orogenic Au deposits. Orogenic Au deposits within the peninsula are structurally controlled, hosted in vein systems within ophiolitic and associated rocks, and related to Siluro-Devonian orogenesis (Salinic and Acadian orogenies; Stog'er Tight, Deer Cove, Pine Cove; Patey and Wilton, 1993; Ramezani et al., 2000). The Au-Ag–bearing VMS deposits of the consolidated Rambler and Ming Camp (e.g., Ming [Main], Ming West, Rambler Main, East Rambler, Big Rambler Pond) are hosted within bimodal to ophiolitic sequences and associated with massive sulfide, and have been moderately metamorphosed and polyphase deformed during the Salinic and Acadian orogenies (Tuach and Kennedy, 1978; Tuach, 1988; van Staal, 2007; Castonguay et al., 2009; van Staal and Barr, 2012). Thus, the Baie Verte Peninsula and the actively mined Au-Ag–bearing Ming VMS deposit provide an important location to address relevant genetic questions regarding the precious metal emplacement in metamorphosed and deformed Au-Ag–bearing VMS deposits.

The Ming VMS deposit is a bimodal-mafic, Cu-Au-(Zn-Ag) VMS deposit hosted within Early Ordovician rocks of the Baie Verte oceanic tract. The deposit was mined for Cu and Au during the late 1970s to early 1980s (Ming Main), and again briefly in the mid-1990s (Ming West). Total production at Ming Main was 4.7 million short tons averaging 2.17% Cu, with some Zn, Au, and Ag. The Ming West deposit was brought into production in October 1995. The deposit was mined in 1995 to 1996, producing 142,173 short tons at 3.98 % Cu, 0.17 oz/ton Au, and 0.44 oz/ton Ag from the upper part of the deposit (Pilgrim, 2009). Since late 2011, Rambler Metals and Mining Canada Ltd has been mining the Ming VMS deposit. Exploration in the early 2000s led to the discovery of new ore zones parallel and along strike to the previously mined area from the Ming Mine main shaft. Four of these zones (1806, 1807, Ming South, and Ming North) have National Instrument 43-101 compliant resources; the highest grades of Cu, Au, and Ag are in the 1806 and 1807 zones. All newly discovered zones have elevated Au grades (measured resources of 1.15 Mt at 2.14 wt % Cu, 2.40 ppm Au, 14.11 ppm Ag, and 0.78 wt % Zn; Pilgrim, 2009), which makes it one of the most Au-Ag rich VMS deposits of the Appalachians in terms of Au grades. Among these four zones, the 1806 zone has the highest Au contents (measured resources of 267,000 tonnes at 0.56 wt % Cu, 4.31 ppm Au, 32.15 pm Ag, and 1.31 wt % Zn), which puts this zone into the small subclass of auriferous or precious metal-rich VMS deposits (Poulsen and Hannington, 1996; Poulsen et al., 2000; Mercier-Langevin et al., 2011). The 1806 zone is also less structurally complex than the other zones and provides an ideal opportunity to evaluate the potential for syngenetic versus orogenic origin for Au-Ag enrichment in the deposit.

In this paper a detailed documentation of the mineralogy, mineral distribution, and mineral chemistry is provided for the 1806 zone of the Ming deposit. The stratigraphic setting was established from drill core descriptions and underground mapping to document the relationships between host rock, ore, alteration, and deformation. Detailed work on ore mineralogy, petrography, and paragenesis was undertaken utilizing standard microscopy and scanning electron microscopy. Additionally, electron probe microanalysis (EPMA) data were obtained from most documented ore minerals. The aims of this paper are to (1) document the complex ore mineralogy, mineral chemistry, and metal zonation of a precious metal-rich VMS lens, (2) discuss the genesis of a precious metal-rich VMS lens through the detailed study of the 1806 zone of the Ming deposit in the context of syngenetic hydrothermal activity versus synorogenic deformation and metamorphism, (3) discuss the influence and role of magmatic volatiles relating to the transport and deposition of precious metals in the VMS environment, and (4) describe the effects of later metamorphism and deformation.

Lithotectonic Setting

Baie Verte Peninsula

The Baie Verte Peninsula in the northwest of Newfoundland is part of the Canadian Appalachians and hosts rocks of both the Humber zone in the west and the Notre Dame subzone of the Dunnage zone in the east (Fig. 1). The Humber zone represents the distal Laurentian cratonic margin, whereas the Notre Dame subzone is interpreted to represent remnant arc, back-arc, and ophiolitic rocks that were formed by suprasubduction in the Cambrian (Lushes Bight) and Early Ordovician (Baie Verte oceanic tract; Hibbard, 1983; Swinden and Thorpe, 1984). The remnant arc exposed in the eastern half of the Baie Verte Peninsula is the Baie Verte oceanic tract, which was formed in the Early Ordovician in the Humber Seaway (van Staal, 2007). The basement of the Baie Verte oceanic tract consists of dominantly ultramafic to mafic (i.e., boninite, pillow basalt, gabbro) and minor felsic (i.e., rhyodacite to rhyolite) rocks and their mafic to felsic volcanosedimentary cover sequences (Hibbard, 1983; Skulski et al., 2009, 2010). These Baie Verte oceanic tract basement rock complexes and their cover sequences are today predominantly exposed in the north-central and eastern part of the Baie Verte Peninsula and separated from each other by Silurian intrusions (Fig. 1). The Pacquet Harbour Group, host of the Ming deposit, is one of these complexes and is divided into a lower and an upper portion. The Early Ordovician lower Pacquet Harbour Group (Baie Verte oceanic tract basement) dominantly consists of low-Ti boninites and basalts with minor rhyodacite to rhyolite (i.e., Rambler rhyolite). The upper Pacquet Harbour Group is the cover sequence of the lower Pacquet Harbour Group and has mixed, mid-Ordovician volcanosedimentary rocks and mafic volcanic rocks (Hibbard, 1983; Skulski et al., 2010). Volcanogenic massive sulfide deposition was coeval with the formation of the basement rocks of the Baie Verte oceanic tract in an arc/back-arc setting (van Staal, 2007). However, the exact timing of precious metal enrichment in the VMS deposits is partly obscured by later metamorphism and deformation. The Baie Verte oceanic tract basement rocks and their cover sequences were emplaced onto the Laurentian margin during the Taconic Orogeny during the diachronous closure

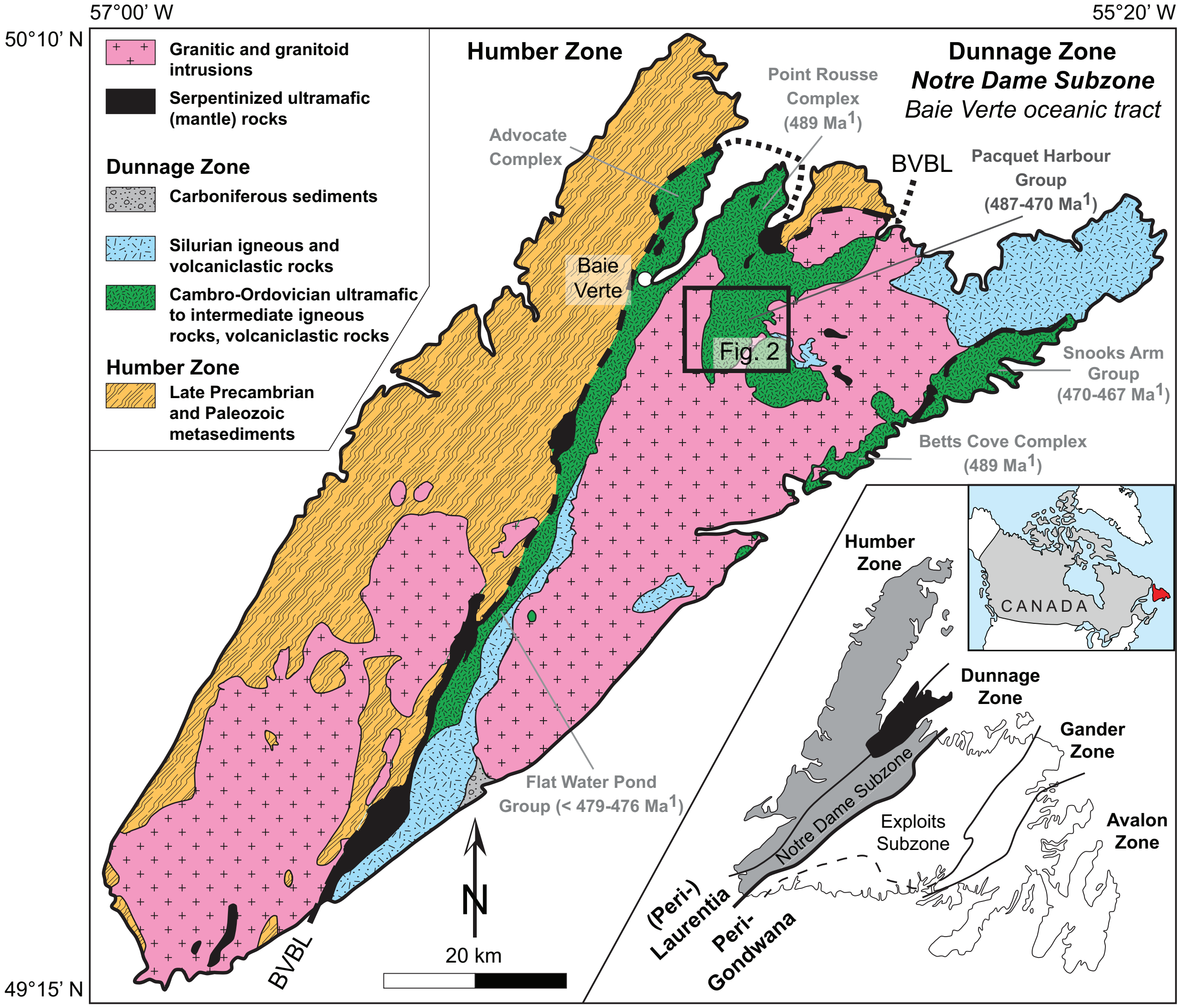

[1]Age data from Castonguay et al. (2009) and Skulski et al. (2010)

FIG. 1. Simplified geologic map from the Baie Verte Peninsula, after Hibbard (1983). Insets in the lower right show the position of Newfoundland (red) within Canada and the various geologic zones of Newfoundland with the contact between (peri-)Laurentia (light gray) and (peri-)Gondwana (white; after Williams, 1979); Baie Verte Peninsula is in black. BVBL = Baie Verte-Brompton Line.

of the Humber Seaway, which resulted in the collision of peri-Laurentian fragments with the Laurentian margin during the mid- to Late Ordovician (Hibbard, 1983; van Staal, 2007; van Staal and Barr, 2012). Subsequent orogenies in the Silurian (i.e., Salinic Orogeny) and Devonian (i.e., Acadian Orogeny) resulted in greenschist to amphibolite facies and polyphase deformation, the formation of orogenic Au deposits, and the emplacement of granitic and granitoid bodies into the Baie Verte oceanic tract (van Staal, 2007; van Staal and Barr, 2012).

The Baie Verte oceanic tract basement rocks and their cover sequences record at least four deformation events (D_1–D_4: Table 1) of varying intensity (Tuach and Kennedy, 1978; Hibbard, 1983; Castonguay et al., 2009, and references therein). The D_2 event, which is associated with the Silurian Salinic Orogeny, is the most prominent in the area and has strongly affected the Ming deposit, resulting in prominent L > S fabrics (30°–35° dip to the northeast of the strata, including the sulfide-bearing horizons) and moderate metamorphism (upper greenschist to lower amphibolite facies; Tuach and Kennedy, 1978; Hibbard, 1983). The D_3 deformation event (Devonian Acadian Orogeny) modified the orientation and geometry of the D_2 structures (Castonguay et al., 2009). The E-W–trending Rambler Brook fault, which is associated with D_2, is located just south of the Rambler rhyolite (Fig. 2).

Consolidated Rambler VMS camp

The Ming (or Ming Main) deposit is one of five VMS deposits (Ming, Ming West, Rambler deposit, East Rambler, Big Rambler Pond) of the consolidated Rambler camp hosted in the lower Pacquet Harbour Group (Fig. 2). The Ming, Ming West, Rambler, and East Rambler deposits are stratabound, bimodal-mafic Cu-(Au) VMS deposits, which were all mined

TABLE 1. Deformation Events Developed in the Pacquet Harbour Group, Baie Verte Oceanic Tract (after Castonguay et al., 2009)

Deformation event	Main characteristic	Effect on Ming mine	Related orogeny
D4	NNE-trending, open to closed upright crossfolds		Alleghenian Orogeny (Permian)
D3	Spaced (in south) to crenulation (in north) foliation, shallowly SE dipping SE-plunging recumbent F_3 folds	Refolding and reorientation down-plunge Potential structural thickening at depth	Acadian Orogeny (Early to mid-Devonian)
D2b	Steep, W-dipping crenulation S-plunging F_2 folds Sinistral transpression during thrusting	Modification to cigar-shaped shafts, dipping 32° to 35° northeast; colinear with the strong NE-plunging L_2 lineation Dismembering and translating of the different zones by thrusting Possible structural thickening of sulfides in hinge zones of regional F_2 folds	Salinic Orogeny (Silurian)
D2a	Main fabric N to NE dipping NE-plunging, closed to isoclinal upright F_2 folds S-directed faults, locally strong NE plunging $L_2 > S_2$ fabric		
D1	Relic fabric		Taconic Orogeny (Ordovician; obduction of ophiolites)

previously (Tuach and Kennedy, 1978; Pilgrim, 2009). Their ore zones are hosted within a moderately metamorphosed and polyphase deformed felsic volcanic footwall (Rambler rhyolite), which yielded a U-Pb zircon age of 487 Ma (unpub. data by V. McNicoll in Castonguay et al., 2009). The sulfide mineralization at Ming, Ming West, and Rambler occurs as semimassive to massive sulfide horizons and sulfide stringers. All three deposits are enriched in Cu and precious metals and dominated by pyrite-chalcopyrite assemblages with lesser pyrrhotite and sphalerite, with variable precious metal enrichment (Tuach and Kennedy, 1978). The hanging-wall rocks of the Ming, Ming West, and Rambler deposits consist of mixed volcanosedimentary and mafic igneous rocks of the ca. 470 Ma upper Pacquet Harbour Group (Skulski et al., 2009, 2010). Rambler East is a small, stratabound, low-grade Cu VMS deposit with minor Au and Ag on the edge of the Rambler rhyolite and shows only stringer and disseminated sulfide mineralization within the silicic footwall (Fig. 2; Tuach and Kennedy, 1978; Swinden and Thorpe, 1984). The sulfide mineral assemblage is pyrite-chalcopyrite-pyrrhotite. The hanging wall consists of siliceous metavolcanic rocks. Tuach and Kennedy (1978) interpreted Rambler East to occur in the same stratigraphic horizon as the Ming and Rambler deposits, but to be formed on the fringes of the Rambler rhyolite.

The Big Rambler Pond deposit is a small mafic Cu VMS deposit located south of the Rambler Brook fault within the boninitic Betts Head Formation of the lower Pacquet Harbour Group and occurs stratigraphically below the Rambler rhyolite (Fig. 2). The deposit shows disseminated and stringer sulfide mineralization of pyrrhotite, chalcopyrite, and pyrite (Tuach and Kennedy, 1978).

The Ming deposit consists of a variety of zones, many discovered since the early 2000s, including the 1806 zone, 1807 zone, Ming South up plunge and down plunge with the Lower Footwall zone, and Ming North (Fig. 3). The 1806 and 1807 zones and Ming South with the Lower Footwall zone run parallel to the old mined shaft, trending northeast with a plunge of 30° to 35°. Ming North is the extension of the old main shaft. All newly discovered horizons are hosted within the Rambler rhyolite. Semimassive to massive and stringer sulfide mineralization is common to all zones except the Lower Footwall zone and consists of pyrite and chalcopyrite with minor sphalerite-pyrrhotite ± arsenopyrite. The Lower Footwall zone contains only chalcopyrite-pyrrhotite ± pyrite stringer mineralization.

Geology of the 1806 Zone

Twenty-three underground drill holes from the 1806 zone (Fig. 3) were examined for stratigraphy, alteration, ore mineralogy, and composition from the up-plunge and down-plunge parts. The terms “up plunge” and “down plunge” are used in this paper to describe two different portions of the 1806 zone relative to the plunge of the zone (Fig. 3) and to highlight the variations (e.g., metal distribution, ore assemblage) between these two areas. Representative graphic drill logs from the 1806 zone are shown in Figure 4. Drill core work was supplemented by underground mapping at the 720 level of the mine in the up-plunge portion of the 1806 zone (Figs. 3, 5). Key aspects of the mineralized succession are summarized below.

Rambler rhyolite

The Rambler rhyolite is a ca. 2.5-km-wide sequence of felsic volcanic rocks of the lower Pacquet Harbour Group and in its upper part is the footwall to the Ming, Ming West, Rambler, and Rambler East deposits (Skulski et al., 2010). The Rambler rhyolite is dacitic to rhyolitic, gray to green with zones with purple hues, is massive to foliated, and is locally intensely altered (Fig. 6a). The thickness of the Rambler rhyolite varies from a few centimeters up to 30 m in drill holes (Fig. 4). The unit consists of various lithofacies including massive flows, rare tuff breccia, and tuff to lapilli tuff (Fig. 4); the contacts between the various lithofacies are gradational. White and blue quartz eyes up to 3 mm commonly occur in all lithofacies. In the down-plunge part of the 1806 zone, quartz eye bearing rhyolite flows predominates whereas, in the up-plunge portion, flows alternate with tuffs to lapilli tuffs (Fig. 4). Rhyolitic lapilli tuff, tuff breccias, and flows are often clast bearing or show remnants of clasts (i.e., ghost clasts). Clasts are usually

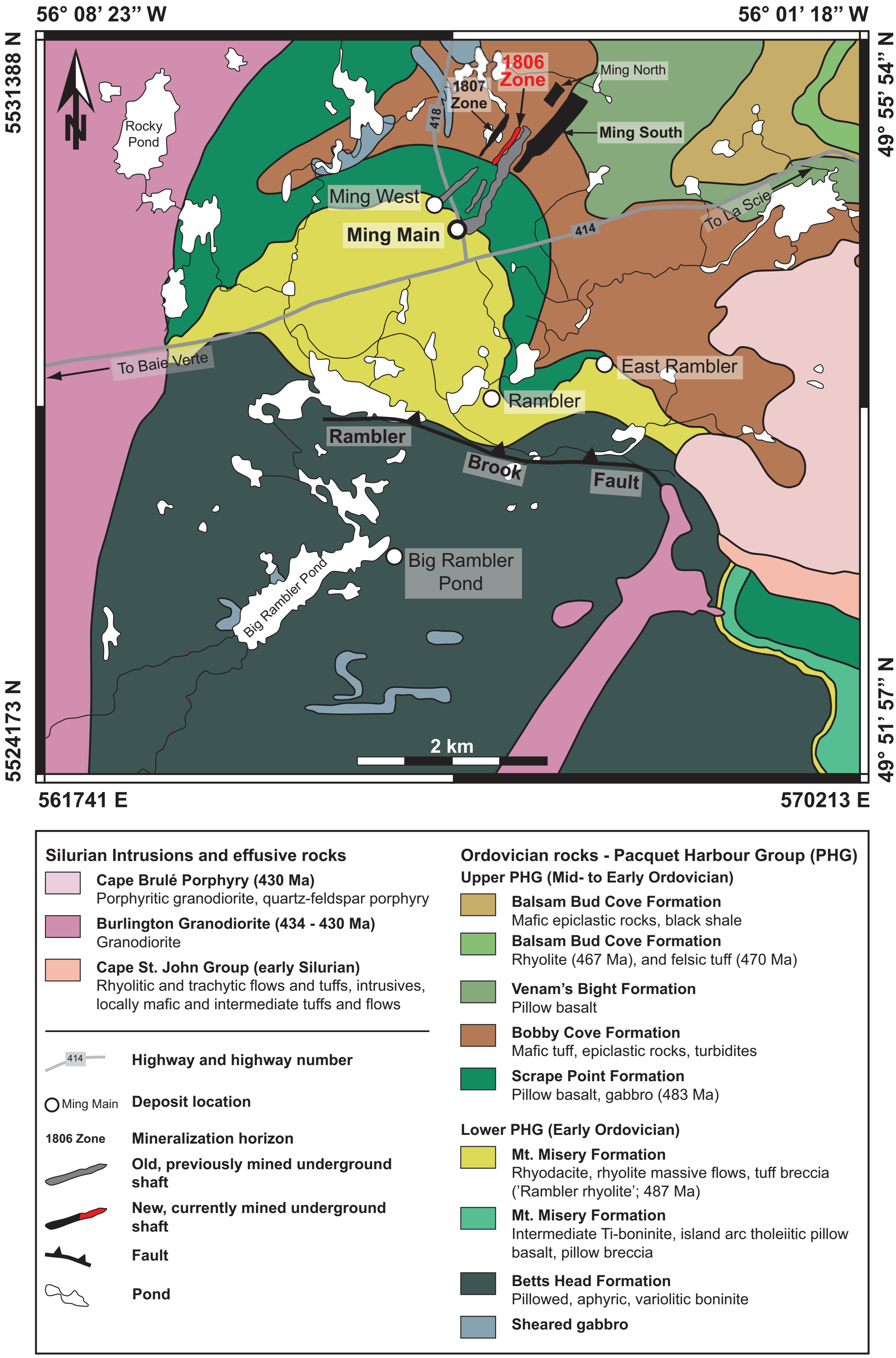

FIG. 2. Detailed geologic map of the Pacquet Harbour Group, hosting the Ming (Main) mine and previously mined volcanogenic massive sulfide deposits (modified after Castonguay et al., 2009); age data for the Pacquet Harbour Group from Castonguay et al. (2009) and Skulski et al. (2010); age data for the Silurian intrusions from Cawood et al. (1993). Datums are shown in WGS 1984 (top and right) and UTM 21N NAD 83 (bottom and left).

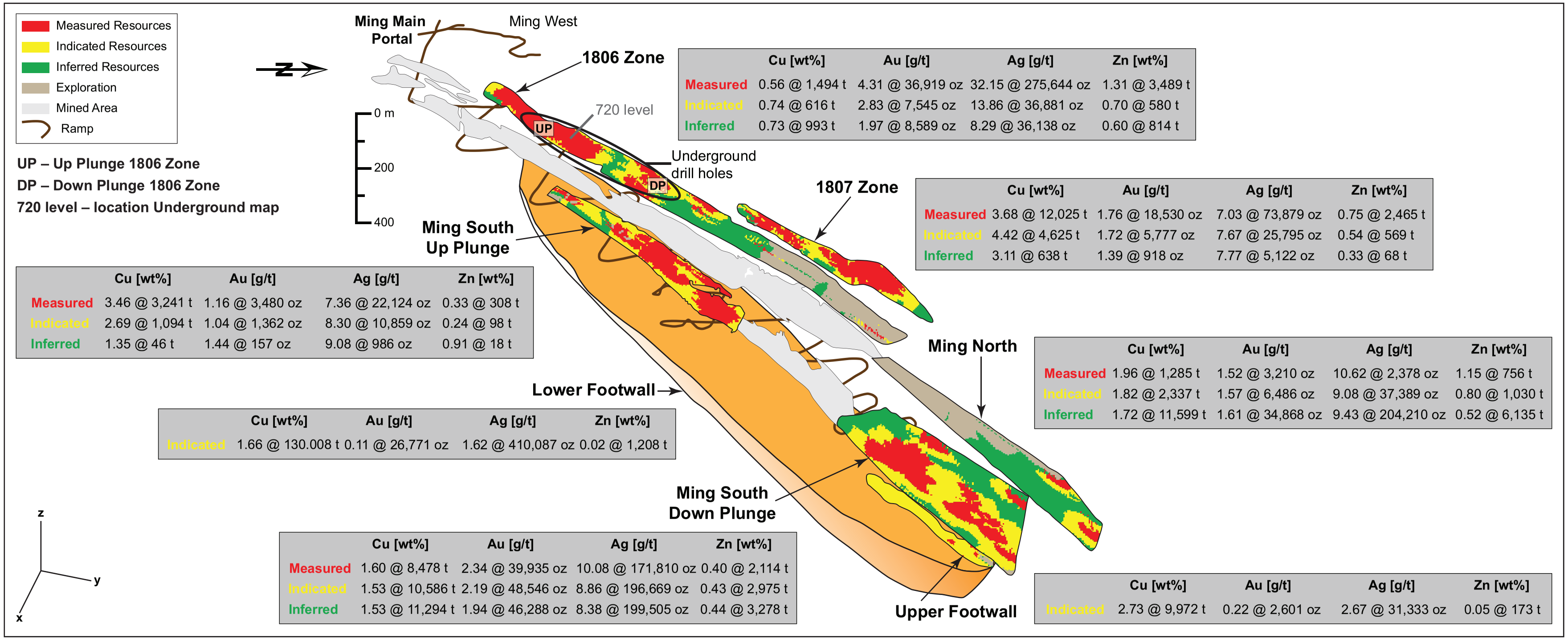

1806 Zone

	Cu [wt%]	Au [g/t]	Ag [g/t]	Zn [wt%]
Measured	0.56 @ 1,494 t	4.31 @ 36,919 oz	32.15 @ 275,644 oz	1.31 @ 3,489 t
Indicated	0.74 @ 616 t	2.83 @ 7,545 oz	13.86 @ 36,881 oz	0.70 @ 580 t
Inferred	0.73 @ 993 t	1.97 @ 8,589 oz	8.29 @ 36,138 oz	0.60 @ 814 t

1807 Zone

	Cu [wt%]	Au [g/t]	Ag [g/t]	Zn [wt%]
Measured	3.68 @ 12,025 t	1.76 @ 18,530 oz	7.03 @ 73,879 oz	0.75 @ 2,465 t
Indicated	4.42 @ 4,625 t	1.72 @ 5,777 oz	7.67 @ 25,795 oz	0.54 @ 569 t
Inferred	3.11 @ 638 t	1.39 @ 918 oz	7.77 @ 5,122 oz	0.33 @ 68 t

Ming South Up Plunge

	Cu [wt%]	Au [g/t]	Ag [g/t]	Zn [wt%]
Measured	3.46 @ 3,241 t	1.16 @ 3,480 oz	7.36 @ 22,124 oz	0.33 @ 308 t
Indicated	2.69 @ 1,094 t	1.04 @ 1,362 oz	8.30 @ 10,859 oz	0.24 @ 98 t
Inferred	1.35 @ 46 t	1.44 @ 157 oz	9.08 @ 986 oz	0.91 @ 18 t

Ming North

	Cu [wt%]	Au [g/t]	Ag [g/t]	Zn [wt%]
Measured	1.96 @ 1,285 t	1.52 @ 3,210 oz	10.62 @ 2,378 oz	1.15 @ 756 t
Indicated	1.82 @ 2,337 t	1.57 @ 6,486 oz	9.08 @ 37,389 oz	0.80 @ 1,030 t
Inferred	1.72 @ 11,599 t	1.61 @ 34,868 oz	9.43 @ 204,210 oz	0.52 @ 6,135 t

Lower Footwall

	Cu [wt%]	Au [g/t]	Ag [g/t]	Zn [wt%]
Indicated	1.66 @ 130.008 t	0.11 @ 26,771 oz	1.62 @ 410,087 oz	0.02 @ 1,208 t

Ming South Down Plunge

	Cu [wt%]	Au [g/t]	Ag [g/t]	Zn [wt%]
Measured	1.60 @ 8,478 t	2.34 @ 39,935 oz	10.08 @ 171,810 oz	0.40 @ 2,114 t
Indicated	1.53 @ 10,586 t	2.19 @ 48,546 oz	8.86 @ 196,669 oz	0.43 @ 2,975 t
Inferred	1.53 @ 11,294 t	1.94 @ 46,288 oz	8.38 @ 199,505 oz	0.44 @ 3,278 t

Upper Footwall

	Cu [wt%]	Au [g/t]	Ag [g/t]	Zn [wt%]
Indicated	2.73 @ 9,972 t	0.22 @ 2,601 oz	2.67 @ 31,333 oz	0.05 @ 173 t

FIG. 3. Resource data for the newly explored zones at the Ming deposit from Rambler Metals and Mining Canada Ltd. (www.ramblermines.com; Pilgrim, 2009); new zones trend northeast and plunge 30° to 35°, parallel to the previously mined area (light gray). The 1806 zone, with its up-plunge and down-plunge portions, is the focus of this paper; the 720 level marks the location of the underground map shown in Figure 5. Resource data are compliant with National Instrument 43-101.

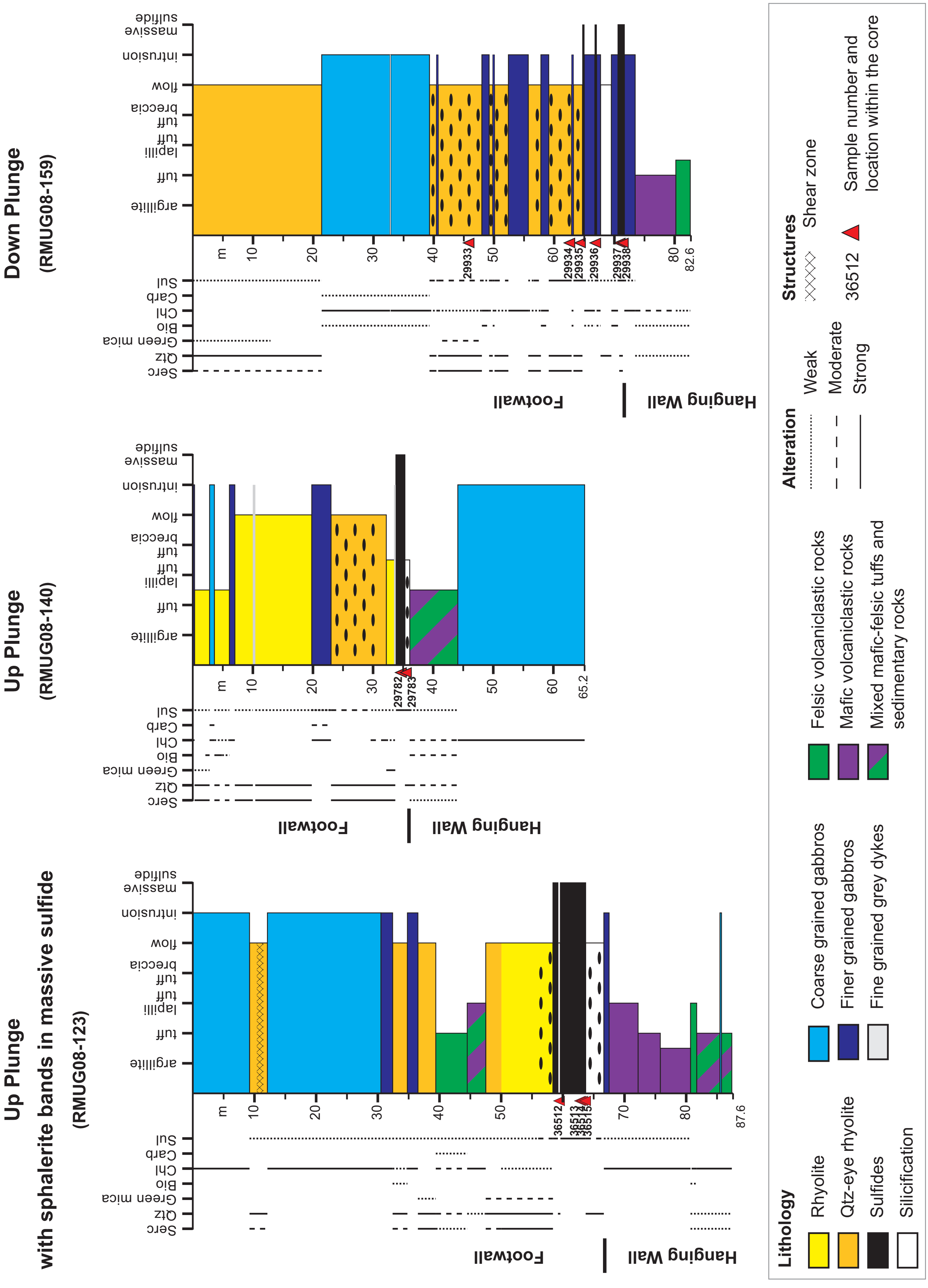

FIG. 4. Stratigraphic drill core sections from the up-plunge and down-plunge portions of the 1806 zone. Drill holes are reversed due to underground drilling, i.e., the beginning of the section represents footwall, and the end hanging wall. Abbreviations: Bio = biotite, Carb = carbonate, Chl = chlorite, Qtz = quartz, Serc = sericite, Sul = sulfides.

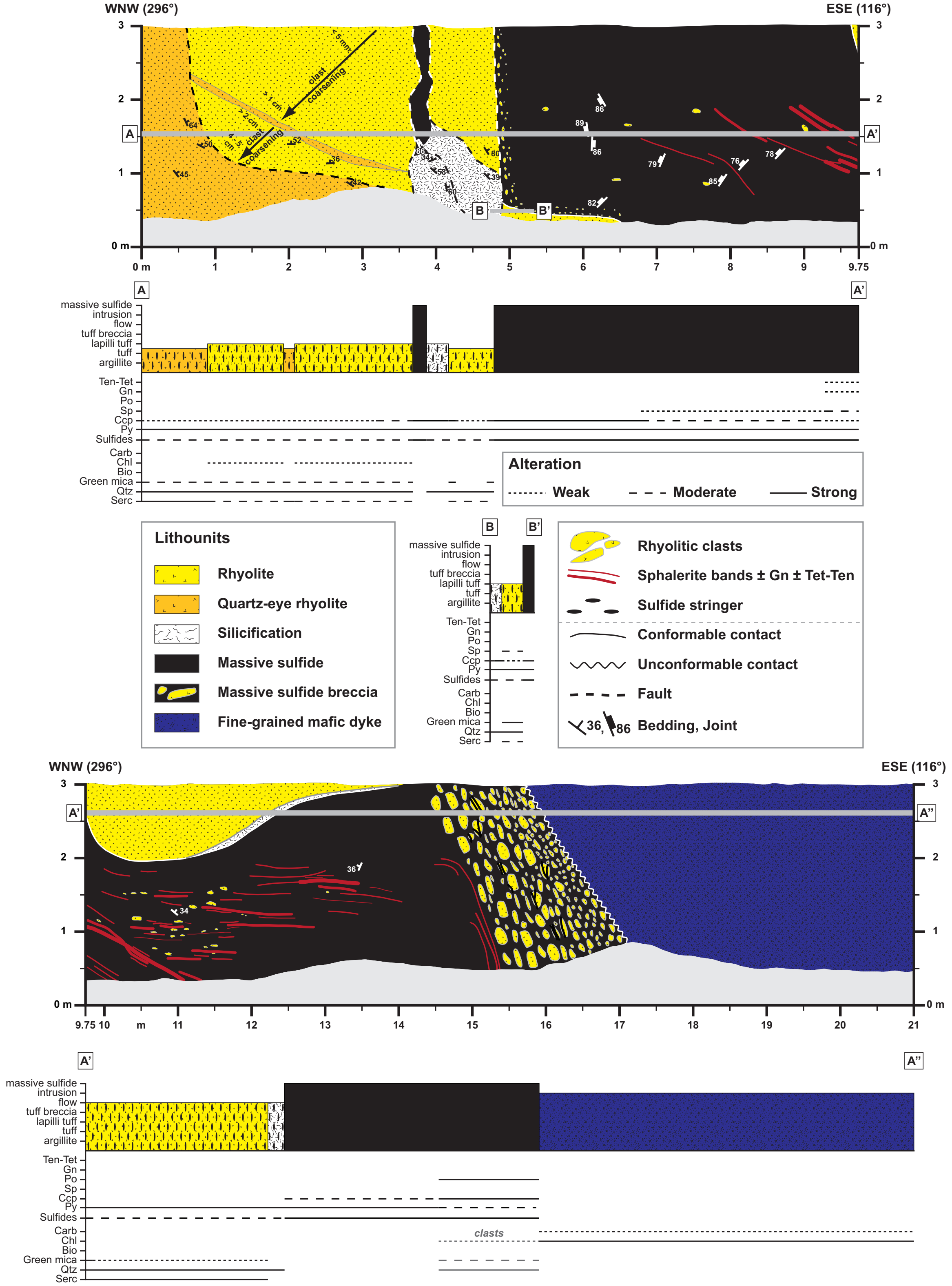

FIG. 5. Underground map from the 720 level (up-plunge portion) of the 1806 zone (Fig. 3). Mapped wall (top: first half, 0–9.75 m; bottom: second half, 9.75–21 m) is a cross section perpendicular to the NE-trending sulfide lens and shows the relationships between the massive sulfide lens (black) and the different rock types (Rambler rhyolite, mafic dike, silicified cap horizon). Hypothetical drill profiles are shown for mapped wall (top: A-A' and B-B', bottom: A'-A") to illustrate variations in lithology, alteration, and sulfide mineralogy; see text for details. Abbreviations: Bio = biotite, Carb = carbonate, Ccp = chalcopyrite, Chl = chlorite, Gn = galena, Po = pyrrhotite, Py = pyrite, Qtz = quartz, Serc = sericite, Sp = sphalerite, Ten-Tet = tennantite-tetrahedrite.

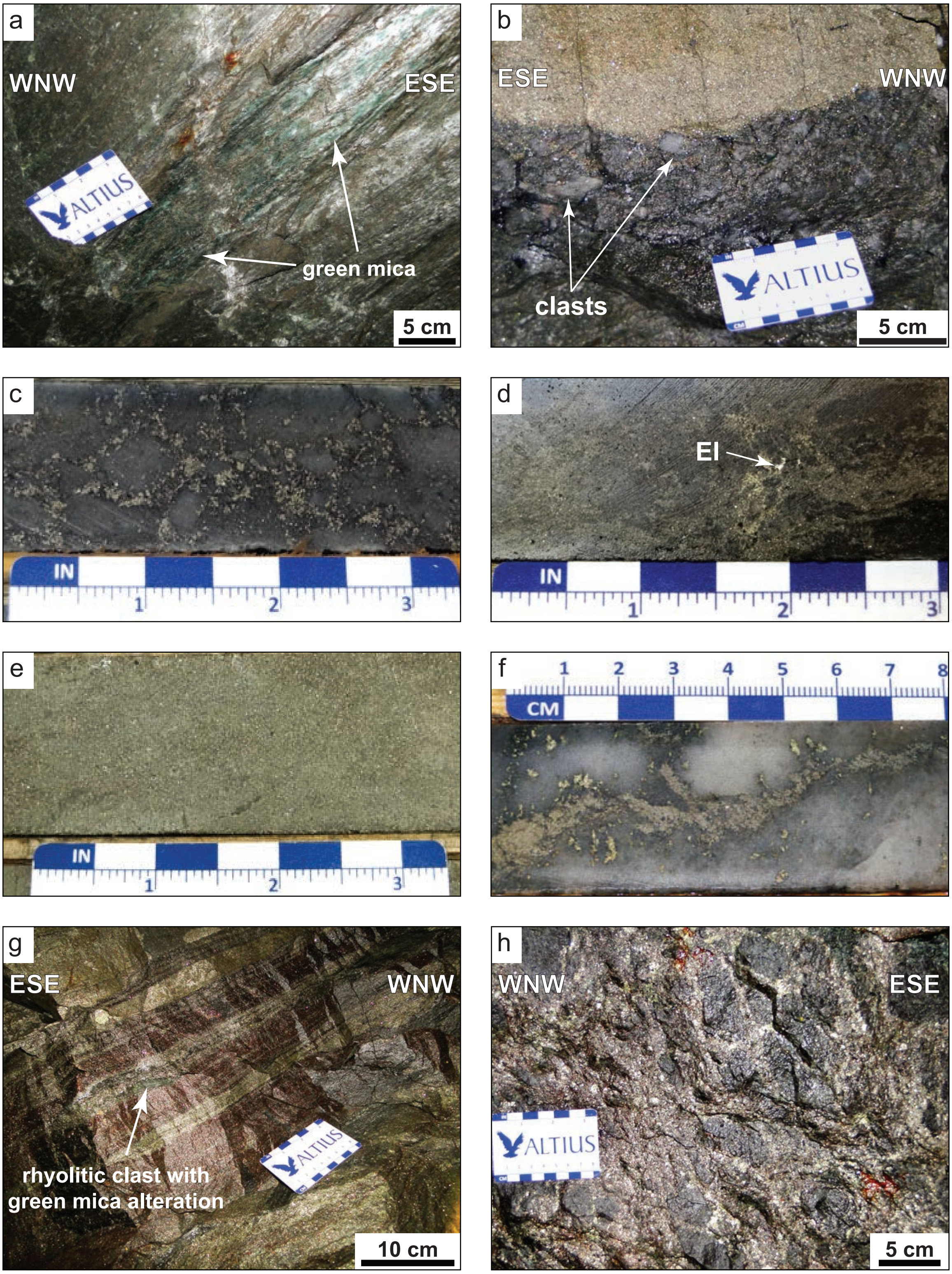

FIG. 6. Rambler rhyolite and sulfide mineralization at the 1806 zone. (a) Altered and deformed Rambler rhyolite with green mica (white arrows). (b) Sharp contact between clast-bearing rhyolitic lapilli tuff to massive sulfide lens. (c) Brecciated pyrite-sphalerite stringer around subrounded, silicified clasts in quartz eye-bearing, rhyolitic lapilli tuff. (d) Stringer sulfides of pyrite-chalcopyrite-sphalerite composition with visible electrum (El; white arrow). (e) Massive pyrite-chalcopyrite sulfide. (f) Silicified horizon with ghost clasts in assumed lapilli tuff and with discordant pyrite-chalcopyrite sulfide stringers. (g) Massive pyrite-chalcopyrite sulfides with sphalerite bands and relict rhyolite clasts with green mica alteration (white arrow). (h) Massive sulfide breccia with coarse, subangular rhyolite clasts in chalcopyrite-pyrrhotite-pyrite matrix on contact with mafic dike. See text for details.

silicified, subangular to subrounded and up to 3 cm in size (Fig. 6b, c). Rhyolitic units with coarse clasts and ghost clasts are found proximal to the semimassive to massive sulfide horizon (Figs. 4, 5, and 6b).

Mineralized zones

The 1806 zone mineralization consists of (1) discordant sulfide stringers in footwall rocks, (2) concordant to stratabound semimassive to massive sulfides, and (3) sulfide veinlets and disseminations in a silicified cap horizon. Stringers (30–50% sulfide in host rock) in footwall rhyolite vary in intensity, but the thickness and abundance of the sulfide veins increase toward semimassive to massive sulfides. Sulfide stringer zones are usually up to 10 m thick but can locally be up to 20 m thick (Fig. 4). The contact with the overlying semimassive and/or massive sulfides is sharp (Fig. 6b). The sulfide veins are composed of pyrite, chalcopyrite, and sphalerite (Fig. 6c). Sulfide stringers are often transposed into the main foliation or have a random orientation around clasts and ghost clasts (Fig. 6c).

The semimassive to massive sulfides consist of more than 50% sulfides with minor, small to coarse, rounded to subangular and altered (quartz, sericite, green mica) rhyolite fragments, and are up to 8 m thick in the 1806 zone. Alternations between semimassive and massive sulfides are common. The semimassive to massive sulfides contain pyrite as the main sulfide phase (Fig. 6d, e), which is associated with lesser amounts of chalcopyrite, sphalerite, and pyrrhotite. Electrum, arsenopyrite, galena, and tetrahedrite are present in minor amounts (Fig. 6d). In the up-plunge portion of the sulfide lens, sphalerite bands with minor galena ± tetrahedrite commonly occur (Figs. 5, 6g). These sphalerite bands are 1 to 30 cm thick and are parallel to the main foliation (Fig. 6g). Sulfides are fine grained, but pyrite can be coarse grained along some mafic dikes due to recrystallization, and underground, near dikes, the sulfides commonly occur in ~2-m brecciated horizons with abundant coarse, subangular and altered rhyolite clasts in a sulfide matrix (Figs. 5, 6h). These brecciated horizons are interpreted to be reworked sulfide breccia due to the replacement of Rambler rhyolite by the mafic dike.

Silicified horizon/silicified rhyolite: A strongly silicified horizon commonly occurs on top of the massive sulfide horizon; however, it is not present in all parts of the zone (Fig. 4). It is usually 30 to 50 cm thick but is locally up to 3 m. This horizon is gray-white, massive, and mineralized with remnants of former coarse rhyolite clasts (Fig. 6f). This ghost clast texture resembles the clast-bearing units of the Rambler rhyolite, occurring usually just below the semimassive to massive sulfide lens (Fig. 6b). The cap usually has a sharp contact with the massive sulfide horizon, consists of random stringers proximal to the massive sulfide horizon, and becomes disseminated sulfide and electrum at distance from the massive sulfide (Fig. 6f). Pyrite and chalcopyrite are the main sulfide phases, but pyrrhotite, arsenopyrite, and visible electrum are also present.

Hanging-wall mafic, felsic, and mixed volcaniclastic rocks

Mafic, felsic, or mixed tuffaceous rocks sit on top of the semimassive to massive sulfide horizon or the silicified cap; they are generally 5 to 10 m in thickness (Fig. 4b, c). The volcaniclastic sequence likely correlates with the upper Pacquet Harbour Group (Skulski et al., 2010). The rocks are light to dark greenish or grayish and alternate between tuff and lapilli tuff. The contacts with the footwall strata and with mafic dikes are sharp. The hanging-wall volcaniclastic rocks are generally finely laminated to thinly bedded and locally exhibit normal grading. The rocks contain a weak foliation, which often results in clast elongation, and only proximal to the mineralization does the unit contain any alteration or mineralization (i.e., fine pyrite). They are interpreted to be distal volcaniclastic turbiditic rocks.

Mafic and felsic dikes

Mafic dikes: Dark greenish, fine- to coarse-grained gabbro dikes cut both the footwall and hanging-wall rocks and range in thickness from a few decimeters up to several tens of meters (Figs. 4, 5). Crosscutting relationships indicate that at least two dike generations are present with fine-grained dikes cutting coarse-grained dikes. Contacts with adjacent rock types are sharp and chilled margins are common in dikes that cut the Rambler rhyolite. The coarse-grained dikes are characterized by coarse biotite, amphibole, and minor feldspar set in a fine-grained greenish matrix. The fine-grained dikes have a similar mineralogy but lack feldspar and do not have any porphyroclasts. Rare pyrite cubes occur in coarse-grained and fine-grained dikes.

Felsic dikes: Very fine grained felsic dikes are not common in the mineralized environment. They occur predominantly in the footwall, cutting the Rambler rhyolite. They are light gray, up to 20 cm thick, and have sharp contacts. Alteration and sulfide mineralization are usually absent and deformation is also not observed.

Hydrothermal alteration

Quartz-sericite ± green mica-sulfide is the dominant footwall alteration assemblage in the Rambler rhyolite (Fig. 6a-c); chlorite and biotite occur sporadically in the Rambler rhyolite. Green mica increases in proximity to mineralization (Figs. 4, 5) and rhyolite clasts in the massive sulfide have green mica alteration (Fig. 6g). The silicified horizon has very strong quartz alteration, with lesser chlorite and sulfide (Figs. 4, 5, 6f). Alteration decreases into the hanging wall and is dominated by chlorite, quartz, and minor biotite ± sericite (Fig. 4).

Sulfide and Oxide Mineralogy

The sulfide and oxide mineralogy of the 1806 zone was examined by optical microscopy of polished thin sections of 86 samples from 23 drill cores. Some research on the sulfide and oxide mineralogy at Ming has been previously documented in Brueckner et al. (2011); however, little work has been reported on sulfide and precious metal mineral textures, precious metal mineral associations, and the spatial variations in sulfide, sulfosalt, oxide, and precious metal minerals in the 1806 zone.

Pyrite (FeS_2), chalcopyrite ($CuFeS_2$), sphalerite (ZnS), pyrrhotite ($Fe_{(1-x)}S$), and galena (PbS) are the main sulfide phases in the 1806 zone (i.e., stringer sulfides, semimassive to massive sulfides, silicified cap horizon). Pyrite is the dominant sulfide phase. Variations in the abundances and distributions of sulfides are shown in Figure 7. In general, chalcopyrite and pyrrhotite are more abundant in the down-plunge portion of the

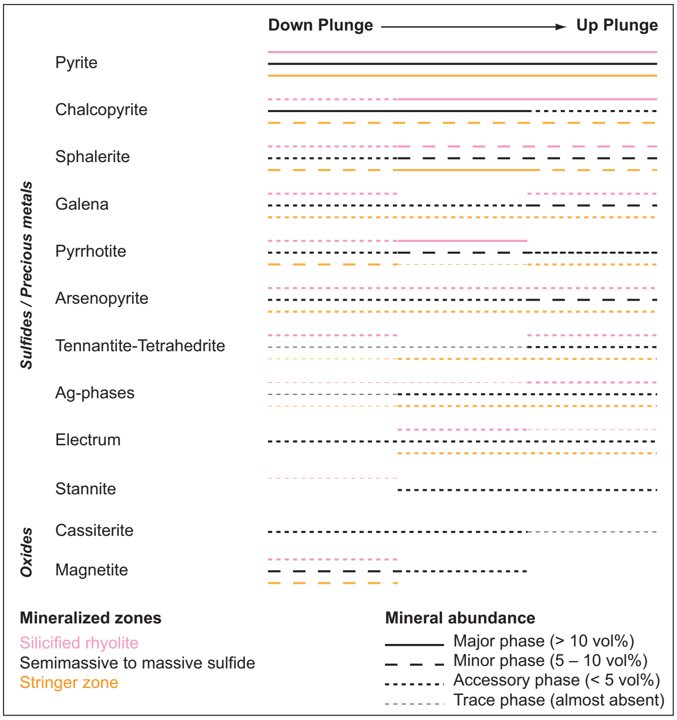

FIG. 7. Sulfide mineral abundance within the 1806 zone from the down-plunge portion to the up-plunge portion for base metal sulfides including arsenopyrite, the most abundant sulfosalts, precious metals, and oxides.

orebody, whereas sphalerite and galena are more abundant in the up-plunge portion of the 1806 zone (Fig. 7). Besides the main base metal sulfides above, there are more than 10 different sulfide, sulfosalt, precious metal, and telluride phases present in the 1806 zone, including arsenopyrite (FeAsS), tennantite ($(\mathrm{Cu, Ag})_{10}(\mathrm{Fe, Zn})_2\mathrm{As}_4\mathrm{S}_{13}$)-tetrahedrite ($(\mathrm{Cu, Ag})_{10}(\mathrm{Fe, Zn})_2\mathrm{Sb}_4\mathrm{S}_{13}$), stannite ($\mathrm{Cu_2FeSnS_4}$), Ag phases (e.g., miargyrite ($\mathrm{AgSbS_2}$), pyrargyrite ($\mathrm{Ag_3SbS_3}$), mercurian stephanite ($(\mathrm{Hg,Ag})_5\mathrm{SbS}_4$)), an unnamed AgCuFeS phase, AgHg alloys, and mercurian electrum (AuAgHg alloy; Fig. 7). The up-plunge portions of the 1806 zone are generally enriched in these phases (Fig. 7).

Arsenopyrite is the most abundant trace to minor phase in the 1806 zone (Fig. 7). Arsenopyrite occurs in three main associations: (1) with base metal sulfides, preferentially with pyrite, chalcopyrite, and pyrrhotite as euhedral to subhedral grains or as inclusions in these phases; (2) intergrown with tennantite-tetrahedrite either as small, euhedral arsenopyrite crystals (Fig. 8a) or as anhedral grains in a myrmekitic texture with additional chalcopyrite ± sphalerite ± electrum ± galena (Fig. 8c-e); and (3) in close proximity to precious metal phases (Fig. 8c-k, m, n). In the down-plunge part, arsenopyrite also occurs with cassiterite. Arsenopyrite shows evidence for recrystallization (e.g., porphyroblast growth; Fig. 8i), but there are wormy-like grains with replacement-like textures containing chalcopyrite (P. Spry, pers. commun., 2013) that are likely original textures (Fig. 8c-e).

Tennantite-tetrahedrite is the most common sulfosalt and occurs throughout the 1806 zone but is preferentially enriched in the up-plunge portion of the lens (Fig. 7). Tennantite-tetrahedrite commonly occurs as large anhedral masses (Fig. 8b, c), often with myrmekitic intergrowth textures with arsenopyrite-chalcopyrite ± sphalerite ± electrum ± galena (Fig. 8c, d). The various sulfide phases and electrum that are present in such myrmekites are most commonly anhedral (e.g., wormy-like, subrounded, amoeboid), with minor exceptions. Electrum is closely associated with or spatially proximal to myrmekitic sulfosalts-sulfides (Fig. 8c-e). In the down-plunge portion of the 1806 zone, tennantite-tetrahedrite occurs predominantly with chalcopyrite and/or arsenopyrite (Fig. 8a). In contrast, in the up-plunge area tennantite-tetrahedrite is associated with arsenopyrite, sphalerite, galena, chalcopyrite, and precious metals (Fig. 8b, e, l). In particular in the sphalerite bands, tennantite-tetrahedrite often replaces chalcopyrite (Fig. 8b).

A wide variety of Ag phases occur predominantly in the up-plunge portion of the 1806 zone (Fig. 7). An AgHg ± Au alloy containing less than 10 wt % Au occurs predominantly along fractures and between grain boundaries of recrystallized pyrite (Fig. 8h). Miargyrite, pyrargyrite, and the other Ag phases are usually associated with electrum (Fig. 8g, m), arsenopyrite (Fig. 8g, j, k), chalcopyrite (Fig. 8g, j), or sphalerite ± galena (Fig. 8k).

Gold occurs either as electrum with elevated Hg concentration (mercurian electrum) or as an AgHgAu alloy with over 10 wt % Au; the former occurrence is by far more abundant than the latter. Associations with base metal sulfides chalcopyrite and pyrite predominate, whereas assemblages with sphalerite, galena, or pyrrhotite are minor and restricted to the up-plunge portion of the 1806 zone (Fig. 8d-g, l-n). Besides base metal sulfides, electrum shows a strong association with arsenopyrite, sulfosalts (e.g., tennantite-tetrahedrite, stannite), and Ag phases and occurs always in the vicinity of one or all of these phases. Electrum occurs in various textures: (1) as free grains with base metal sulfides, arsenopyrite, sulfosalts, and/or Ag phases, (2) as inclusions in arsenopyrite, galena, and pyrrhotite, and (3) in myrmekite texture in tennantite-tetrahedrite.

Stannite is an accessory phase and is commonly restricted to the semimassive to massive sulfide horizon in the up-plunge portion of the deposit (Fig. 7). It occurs with sphalerite (Fig. 8j, k) and/or chalcopyrite (Fig. 8k). Stannite (with or without cassiterite inclusions) occurs exclusively in Ag phases and/or electrum-bearing samples and is found proximal to precious metal phases (Fig. 8j, k).

Boulangerite ($\mathrm{Pb_5Sb_4S_{11}}$), loellingite ($\mathrm{FeAs_2}$), bismuth tellurides, coloradoite (HgTe), molybdenite ($\mathrm{MoS_2}$), and unknown sulfide phases (Ni and Sb bearing) are also present in the semimassive to massive sulfides of the 1806 zone. Magnetite ($\mathrm{Fe_3O_4}$) and cassiterite ($\mathrm{SnO_2}$) are more abundant in the down-plunge part of the 1806 zone and are almost entirely absent in the up-plunge part (Fig. 7; see also Brueckner et al., 2011).

Mineral Chemistry

Analytical Methods

Bulk metal analysis: Copper, Zn, Pb, Ag, and Au assay data were obtained from the assay database of Rambler Metals and Mining Canada Ltd. Samples were analyzed at Activation Laboratories, Ancaster, ON. Copper, Zn, Pb, and Ag were analyzed by applying aqua regia with an inductively coupled plasma (ICP) finish (ActLabs Code 1E3). Activation

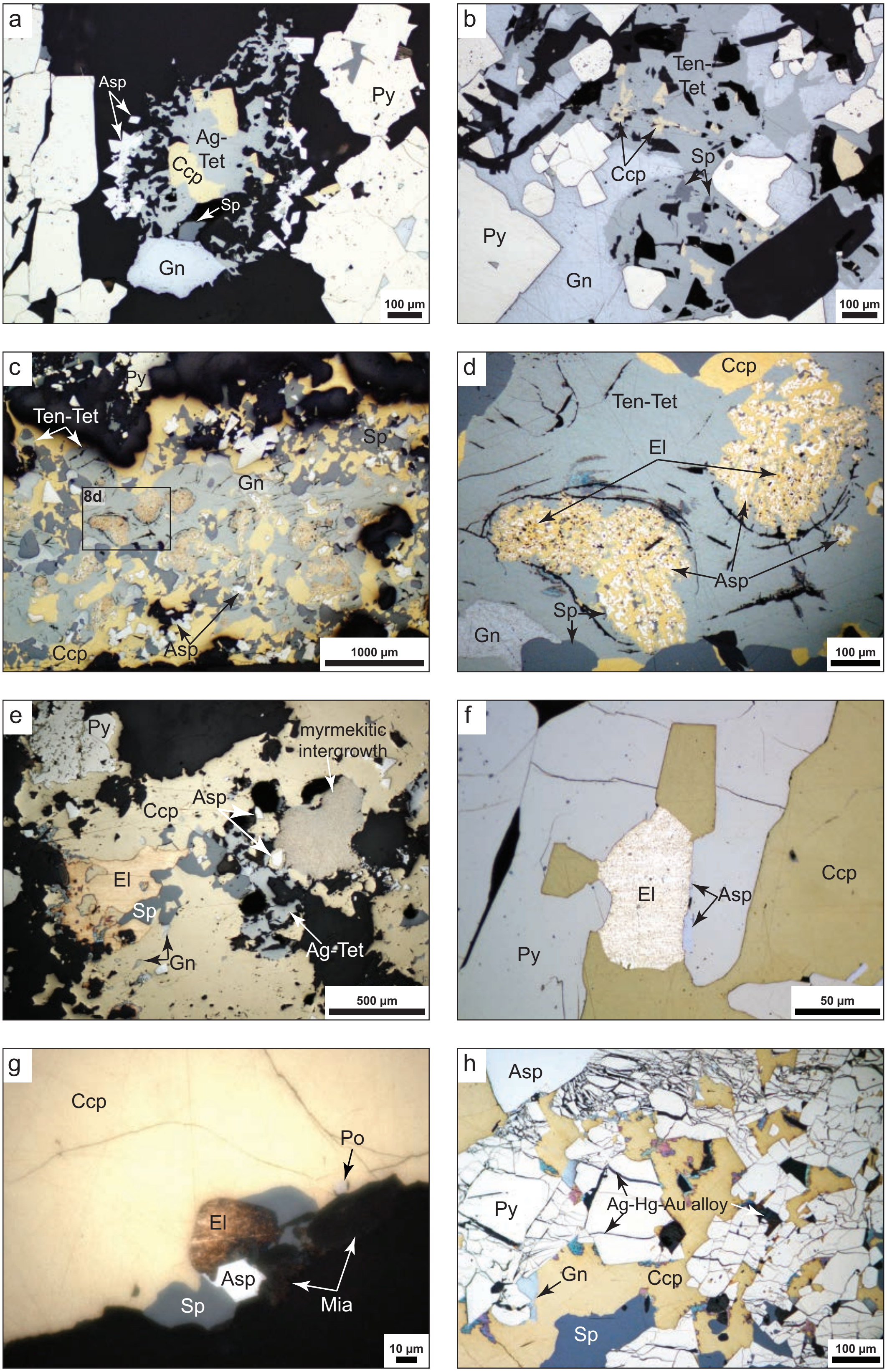
a
Asp
Py
Ag-
Tet
Ccp
Sp
Gn
100 µm
b
Ten-
Tet
Ccp
Sp
Py
Gn
100 µm
c
Py
Ten-Tet
Sp
Gn
8d
Ccp
Asp
1000 µm
d
Ccp
Ten-Tet
El
Asp
Sp
Gn
100 µm
e
Py
myrmekitic
intergrowth
Asp
Ccp
El
Sp
Gn
Ag-Tet
500 µm
f
El
Asp
Ccp
Py
50 µm
g
Ccp
Po
El
Asp
Sp
Mia
10 µm
h
Asp
Py
Ag-Hg-Au alloy
Gn
Ccp
Sp
100 µm

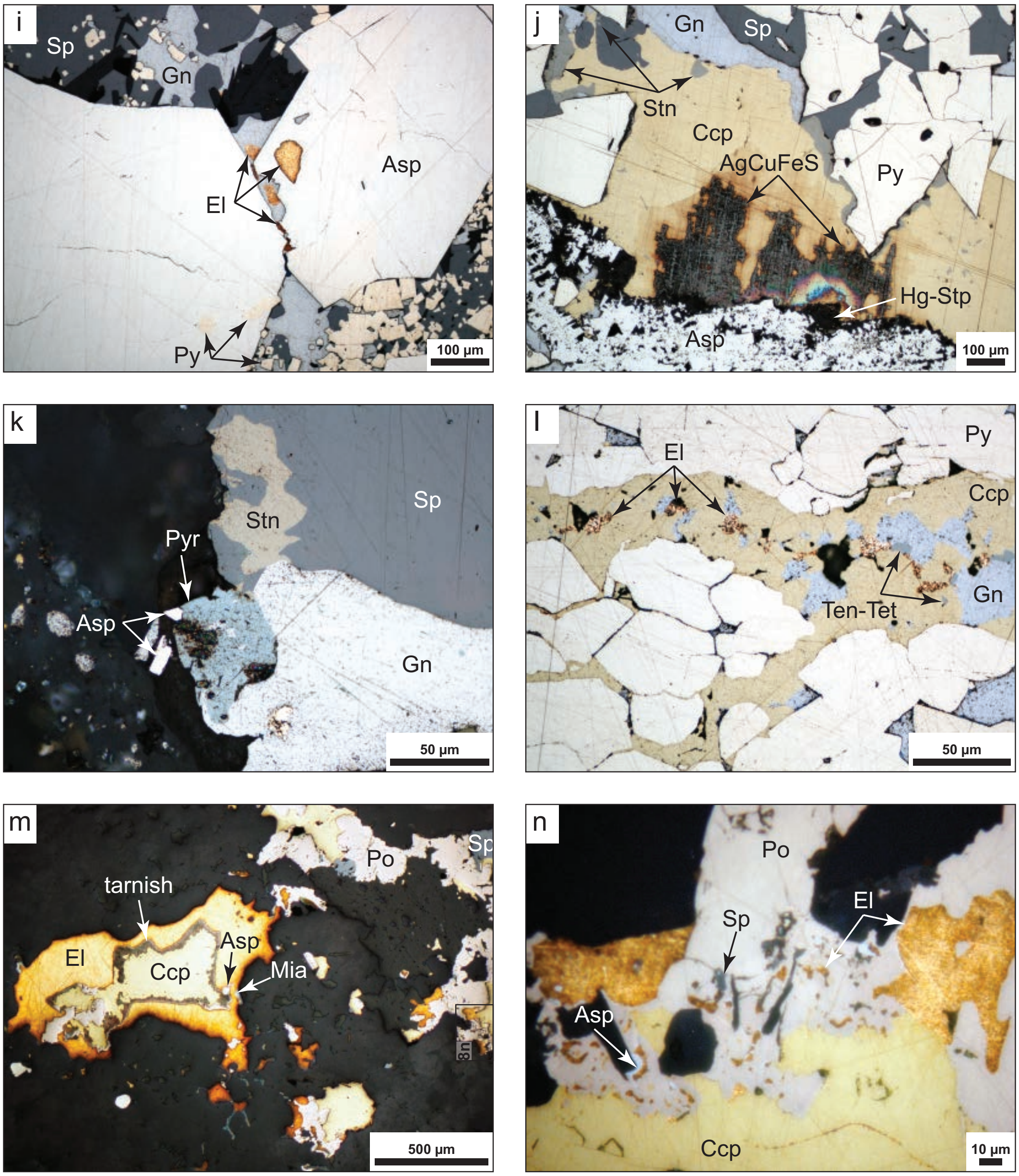

FIG. 8. Reflected light images of sulfide assemblages and textures from semimassive to massive sulfides (a, b, f-l), sulfide stringer (c-e), and silicified horizon (m, n). (a) Intergrowth of Ag-bearing tetrahedrite with chalcopyrite and marginal arsenopyrite (semimassive sulfide, down-plunge). (b) Tennantite-tetrahedrite replacing chalcopyrite and partly intergrown with sphalerite and galena marginal to tennantite-tetrahedrite (massive sulfide, up-plunge). (c) Tennantite-tetrahedrite with myrmekite textures of arsenopyrite-chalcopyrite-sphalerite-tennantite-tetrahedrite ± sphalerite ± electrum and marginal chalcopyrite-arsenopyrite-sphalerite-galena (sulfide stringer on contact to massive sulfide, up-plunge). (d) Detail from c: small, subroundish electrum in myrmekite (black arrows; sulfide stringer on contact to massive sulfide, up-plunge). (e) Electrum with marginal sphalerite in chalcopyrite and in close spatial relation to Ag-bearing tetrahedrite and very fine grained myrmekite (sulfide stringer, up-plunge). (f) Electrum with marginal arsenopyrite between recrystallized pyrite in chalcopyrite (semimassive sulfide, down-plunge). (g) Small, roundish electrum with arsenopyrite-miargyrite-sphalerite marginal to chalcopyrite (semimassive sulfides, up-plunge). (h) Brittle deformed and recrystallized pyrite with Ag-Hg-Au alloy along cracks and between pyrite grain boundaries; arsenopyrite porphyroblast close to precious metals (massive sulfide, up-plunge). (i) Electrum inclusions in galena and arsenopyrite porphyroblast (massive sulfide, up-plunge). (j) Unnamed AgCuFeS phase and mercurian stephanite in chalcopyrite on contact to intergrowth of arsenopyrite-pyrite and close to stannite (massive sulfide, up-plunge). (k) Pyrargyrite with arsenopyrite and galena margin; sphalerite with stannite inclusion (massive sulfide, up-plunge). (l) Small, subroundish electrum with galena and tennantite-tetrahedrite in chalcopyrite (massive sulfide, up-plunge). (m) Coarse electrum enclosing chalcopyrite-pyrrhotite-arsenopyrite and with marginal miargyrite in quartz; fine rim of tarnish on chalcopyrite-electrum contact (silicified horizon, up-plunge). (n) Detail of 8 m: electrum as inclusions in and marginal to pyrrhotite; arsenopyrite and sphalerite inclusions in pyrrhotite (silicified horizon, up-plunge). See text for details. Mineral abbreviations: AgCuFeS = unnamed AgCuFeS phase, Ag-Tet = Ag-bearing tetrahedrite, Asp = arsenopyrite, Ccp = chalcopyrite, El = electrum, Gn = galena, Hg-Stp = mercurian stephanite, Mia = miargyrite, Po = pyrrhotite, Py = pyrite, Pyr = pyrargyrite, Sp = sphalerite, Stn = stannite, Ten-Tet = tennantite-tetrahedrite.

Laboratories used a fire assay fusion followed by acid digestion and analyses by atomic absorption for Au analyses (ActLabs code 1A2). If Au assay exceeded 3,000 ppb and/or Ag exceeded 100 ppm, the samples were treated by fire assay, nitric acid, and a gravimetric finish (ActLabs code 1A3). Quality assurance at Activation Laboratories was obtained by the analysis of certified reference materials. The results were in good agreement with the certified values (Pilgrim, 2009). Moreover, blanks were analyzed for quality assurance and no contamination was reported. More detailed information about the analytical procedure and the obtained results of the reference materials is presented in Pilgrim (2009).

Semiquantitative energy-dispersive X-ray (EDX) imaging/spectroscopy: Backscattered electron (BSE) images and element maps were obtained using an FEI Quanta 400 scanning electron microscope (SEM) at the Bruneau Innovation Centre at Memorial University of Newfoundland, Canada. The FEI Quanta 400 is equipped with a Bruker silicon drift energy dispersive X-ray (EDX) detector. This system allows quick semiquantitative detection of a variety of elements (here: Si, S, Fe, Cu, Zn, As, Ag, Au, Hg, Sb, and Sn), element maps, and EDX spectra for numerous phases and to corroborate textures documented using reflected light microscopy. The FEI Quanta 400 was run at high vacuum mode at beam energy of 20 keV and a beam current of 10 nA. A scintillator detected the Kα emission lines of Si, S, Fe, Cu, Zn, and As and the Lα emission lines of Ag, Au, Hg, Sb, and Sn. The Esprit software from Bruker (version 1.9) was used for processing of BSE and EDX data. Elemental maps done via EDX do not give specific concentrations for analyzed elements and are semiquantitative based on raw counts per second. Hence, the measured intensity for each element is proportional to its concentration. Therefore, EDX scans allow detecting the occurrence of elements within minerals. In order to detect possible interferences (e.g., Zn Kβ interferes with Au Lα; As Kα interferes with Pb Lα), the mineral of interest is scanned and alternative emission lines are then used to check if elemental overlaps occur or not. If an overlap occurs, the alternative, interference-free emission line is used for semiquantitative EDX scans.

Electron probe microanalysis (EPMA): A total of 13 samples representing all mineralized zones of the 1806 zone were analyzed for major, minor, and trace composition in sulfides, sulfosalts, precious metal alloys, and oxides at the University of Toronto (UT) using a Cameca SX50/51 electron microprobe. A brief sample description including the mineral assemblage and the analyzed phases in each sample is found in Appendix A1. A total of 17 elements (Ag, As, Au, Bi, Co, Cu, Fe, Hg, Mn, Mo, Ni, Pb, S, Sb, Sn, Te, Zn) were analyzed in each of the 17 phases (e.g., pyrite, chalcopyrite, sphalerite, galena, pyrrhotite, arsenopyrite, tennantite-tetrahedrite, miargyrite, pyrargyrite, mercurian stephanite, unnamed AgCuFeS phase, electrum, stannite, boulangerite, molybdenite, cassiterite, magnetite). The Cameca SX-50/51 is equipped with three tunable wavelength-dispersive spectrometers and a Link (Oxford) Pentafet EDS detector with Be window and a pulse processor. During the measurements in April 2011 and January 2012, beam energy of 25 keV and beam current of 20 nA at a beam diameter of 1 μm were applied. The takeoff angle was 40°. The measured elements were analyzed either by a LIF crystal (Fe Kα, Cu Kα, Zn Kα, As Kα, Te Lα, Hg Lα, Mn Kα, Co Kα, Ni Kα) or PET crystal (Sn Lα, Pb Mα, Bi Mα, S Kα, Mo Lα, Au Mα, Ag Lα, Sb Lα). Counting times were 20 s for Fe Kα, S Kα, Cu Kα, Zn Kα, Pb Mα, Au Mα, Ag Lα, Sb Lα Sn Lα, Te Lα, Bi Mα, Hg Lα, Mo Lα, and 40 s for As Kα, Mn Kα, Co Kα, Ni Kα. Off-peak counting times were identical to the counting time. Detection limits for each element are found in Appendix A2. The detection limit for all analyzed phases is similar for measurements done in April 2011 and January 2012. Quality control was maintained by utilizing UT internal standards for each analyzed phase; calibration standards were measured at the beginning of the phase in question. Measured values on each applied internal standard are in accordance with the accepted concentrations in these standards (pers. comm., Y. Liu, 2013). Additionally, data were deemed acceptable if analytical totals fell within a range of 100 ± 1.5 wt % and their stoichiometry represented the accepted mineral composition. All clean analyses of sulfide and precious metals fell within this range or were otherwise discarded. For oxides the oxygen concentration was calculated and assured via stoichiometry. Accuracy of results was monitored via UT in-house standards. The results above detection limit were within 5% of the accepted values. Moreover, wavelength scans of unknown samples were undertaken to see background conditions as well as potential peak overlaps and interferences and to check the quality of minor element peaks within the unknowns. Precision of the analysis was calculated from the counting rate and is below 0.4% for all major elements; precision for minor components is between 5 and 33%. However, precision increases with increasing concentrations for minor components. Unknown and standard intensities were corrected for dead time. Standard intensities were corrected for standard drift over time by internal software corrections. Interference corrections were applied to S for interference by Co, to As for interference by Pb, to Sn for interference by Co, to Bi for interference by Au, to Mo for interference by Pb, and to Mn for interference by Hg.

Results

Assay data (Activation Laboratories): Assay data for Cu, Zn, Pb, Ag, and Au presented in Figure 9 are from the semimassive to massive sulfide lens of three drill holes (Fig. 4) from the up- and down-plunge portions of the 1806 zone (Table 2). In general, the down-plunge part of the zone is enriched in Cu, whereas the up-plunge portion of the zone (Fig. 9a) is enriched in Zn, Pb, Ag, and Au, reflecting the dominant minerals in each portion of the zone (Fig. 7). In Figure 9b the metal distribution within the massive sulfide lens of drill hole RMUG08-123 (Fig. 4) is shown in detail and this largely reflects the varying amounts of sphalerite and galena (e.g., Zn, Pb enrichments) versus chalcopyrite (e.g., Cu enrichments). The up-plunge portion of the 1806 zone is enriched in gold and, while this zone is also enriched in Zn-Pb, Au is associated with Cu (i.e., chalcopyrite).

Semiquantitative energy-dispersive X-ray: Two samples from the stringer zone and the massive sulfide lens in the up-plunge portion are used to illustrate the close textural and chemical relationships between precious metals (e.g., electrum, Ag phases), arsenopyrite, and various sulfosalts (e.g., Ag-bearing tennantite-tetrahedrite, stannite, boulangerite).

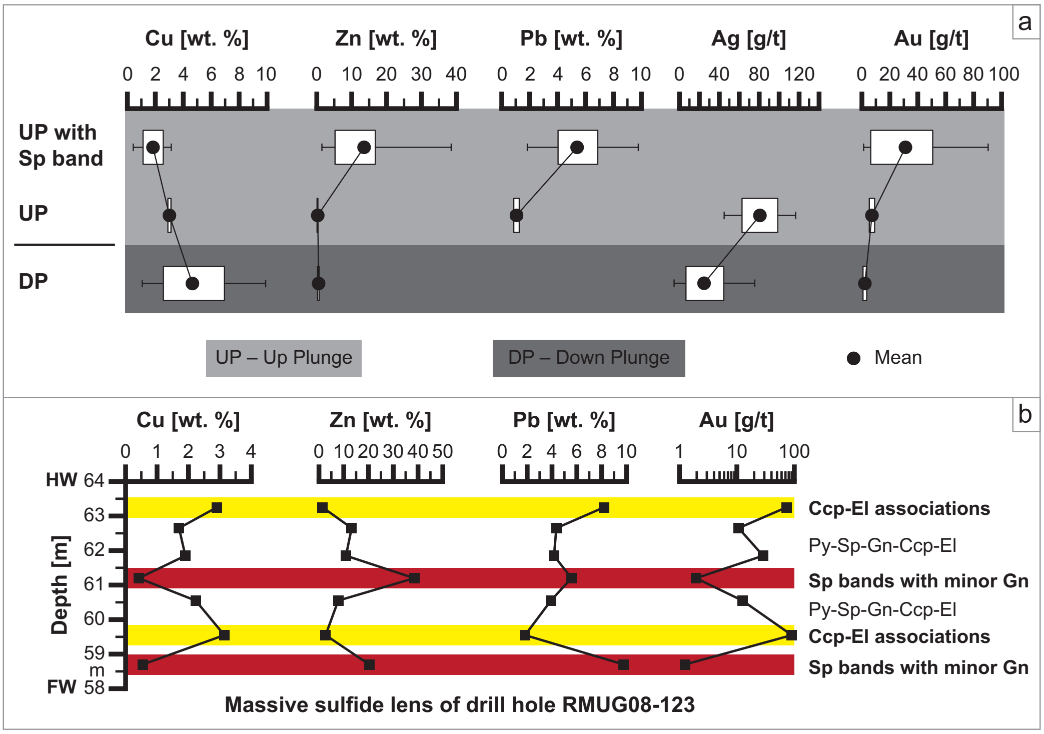

FIG. 9. Metal zoning in the semimassive to massive sulfide lens of the 1806 zone. (a) Box-whisker plot showing variation in base and precious metal grades from the down-plunge (DP) to the up-plunge (UP) portion. (b) Variations in Cu, Zn, Pb, and Au grades within the massive sulfide lens of the uppermost portion of the up-plunge area due to the occurrence of sphalerite bands. See text for details; mineral abbreviations are the same as in Figure 8. Assay data from Rambler Metals and Mining Canada Ltd (www.ramblermines.com; Pilgrim, 2009).

TABLE 2. Assay Data for Cu, Zn, Pb, Ag, and Au of the Semimassive to Massive Sulfide Lens from Three Representative Drill Holes (data from Rambler Metals & Mining Canada Ltd.)

Sample no.	From (m)	To (m)	Ag (ppm)	Au (ppm)	Cu (wt %)	Pb (wt %)	Zn (wt %)
Up Plunge with Sp bands (RMUG08-123)							
27423	58.4	59.1		1.25	0.543	9.78	20.30
27425	59.1	60.1		90.40	3.14	1.83	2.68
27426	60.1	61.1		12.50	2.23	3.91	7.78
27427	61.1	61.4		1.95	0.420	5.57	38.50
27428	61.4	62.4		28.60	1.90	4.16	10.90
27429	62.4	63.0		10.70	1.70	4.35	13.20
27431	63.0	63.6		72.80	2.90	8.18	1.47
	Average			31.17	1.83	5.40	13.55
	Std			35.97	1.06	2.72	12.73
Up Plunge (RMUG08-159)							
28104	33.8	34.7	134.20	11.00	2.79	1.45	0.364
28106	34.7	35.5	62.50	3.40	3.23	0.667	0.180
	Average		98.35	7.20	3.01	1.06	0.272
	Std		50.70	5.37	0.311	0.554	0.130
Down Plunge (RMUG08-159)							
29259	64.1	64.5	93.20	4.20	9.90		0.840
29262	64.7	65.0	74.40	0.800	8.20		0.730
29264	66.6	67.0	24.50	4.16	3.20		0.410
29271	70.6	71.0	25.30	1.01	2.37		0.410
29272	71.0	71.3	12.30	1.18	1.06		0.330
29273	71.3	71.5	24.50	1.37	3.20		0.440
	Average		42.37	2.12	4.66		0.527
	Std		33.00	1.61	3.53		0.206

Abbreviations: Sp = sphalerite, Std = standard deviation

Energy-dispersive X-ray data for a fairly large grain of electrum (>500 μm) from the stringer zone of the 1806 zone associated with chalcopyrite and sphalerite (Figs. 8e, 10a, b) show the association of Au (Fig. 10c), Ag (Fig. 10d), and Hg (Fig. 10e) in electrum. Generally, Au occurs in the core of the grain, whereas Ag is present on the edges (Fig. 10c, d); electron microprobe analyses support the latter and show a weak correlation of Au with Hg (Fig. 10e). There is a close spatial and chemical relationship between sulfosalts and precious metals (i.e., arsenopyrite and Ag-bearing tetrahedrite in close proximity [<500 μm] to electrum; Fig. 10f).

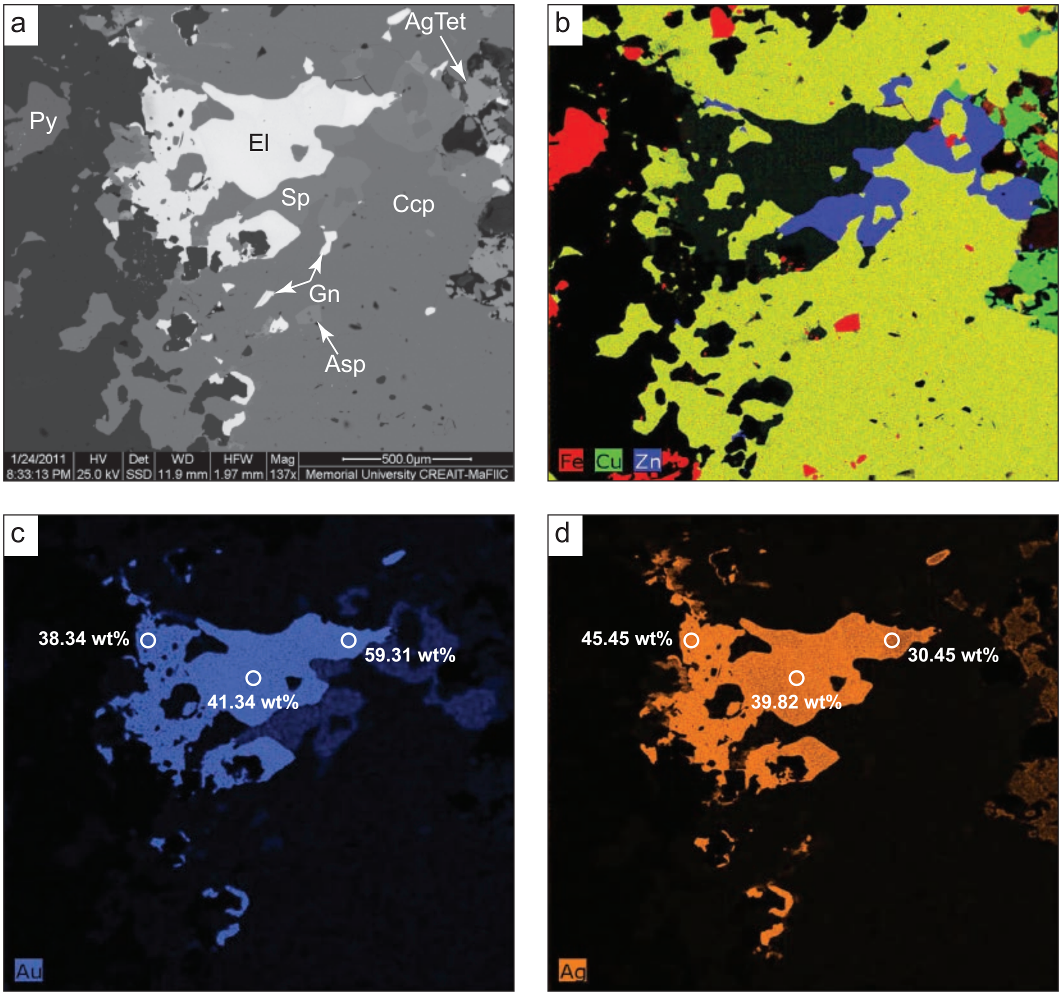

FIG. 10. Backscattered electron (BSE) images and EDX scans done by SEM on two precious metal samples from the up-plunge area for selected elements. Semiquantitative EDX images give the relative occurrence of the measured elements, because only raw data are counted. Interferences and/or background are recognized by running an element (i.e., Cr) that is not known to occur in the measured area. Mineral abbreviations as in Figure 8. (a-f) Electrum in stringer zone (see Fig. 8e). (a) BSE image. (b) EDX scan of Fe, Cu, Zn highlighting pyrite and arsenopyrite (i.e., Fe = red), chalcopyrite (i.e., Cu + Fe = yellow), Ag-bearing tetrahedrite (i.e., Cu = green), and sphalerite (i.e., Zn = blue). (c) EDX scan of Au highlighting the occurrence of electrum (dark blue); white open circles present EPMA data points and measured concentrations, respectively. Note: Au Lα (electrum) interferes with Zn K$_\beta$ (sphalerite), causing a weak blue where sphalerite occurs. (d) EDX scan of Ag highlighting the occurrence of Ag in electrum (center) and Ag-bearing tetrahedrite (right side); white open circles and numbers present EPMA data points and values, respectively. (e) EDX scan of Hg showing the occurrence of Hg in electrum; white open circles and numbers present EPMA data points and values, respectively. (f) EDX scans of As (turquoise) and Sb (yellow), highlighting the presence of arsenopyrite and Ag-bearing tetrahedrite close to electrum. Note: As K$_\alpha$ (arsenopyrite) interferes with Pb L$_\alpha$ (galena) and Au L$_\beta$ (electrum), resulting in a false color for electrum. (g-j) Ag phases and stannite in massive sulfides (see Fig. 8j). (g) BSE image. (h) EDX scan of Fe, Cu, Zn, Ag highlighting pyrite and arsenopyrite (i.e., Fe = red), chalcopyrite (i.e., Fe, Cu = greenish-yellow), stannite (i.e., Cu = lime green), sphalerite (i.e., Zn = blue), an unnamed AgCuFeS phase (i.e., Fe + Cu + Ag = orange to yellow), and mercurian stephanite (i.e., Ag = orange); intensity of Ag (orange) varies within the unnamed AgCuFeS phase. (i) EDX scan of Cu, Hg, As, Zn, Ag showing the occurrence of Hg in stephanite (i.e., Ag + Hg = rose); mercurian stephanite occurs marginal to and within arsenopyrite-pyrite. Note: As K$_\alpha$ (arsenopyrite) interferes with Pb L$_\alpha$ (galena), resulting in some color for both arsenopyrite and galena. (j) EDX scan of Si, Sn, and Ag, showing the close textural and chemical relationship between Ag phases (i.e., Ag = orange) and stannite (i.e., Sn = dark blue in upper half of image); concentration of Ag in the unnamed AgCuFeS phase decreases proximal to mercurian stephanite. Note: Sn L$_\alpha$ interferes with Ca K$_\alpha$ and K K$_\alpha$ emission lines (i.e., light blue in lower half). See text for details.

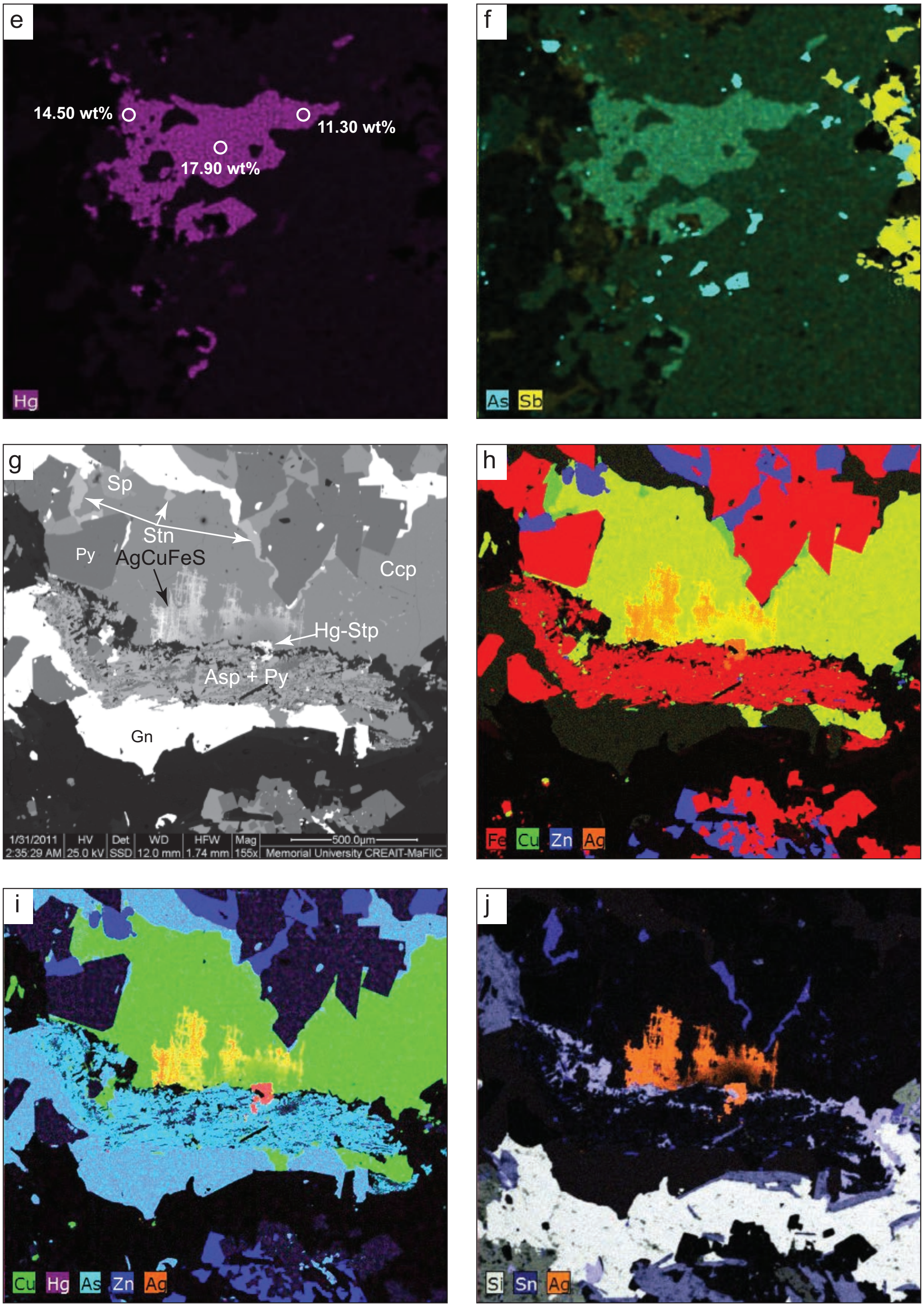

FIG. 10. *(Cont.)*

In addition to electrum, Ag phases are also associated with base metal sulfides, arsenopyrite, and sulfosalts as documented in a sample from the massive sulfide lens (Fig. 10g-j). Moreover, EDX scans of Ag phases also have an association with Hg (e.g., mercurian stephanite; Fig. 10i).

Electron probe microanalysis: Data from selected samples from the up- to the down-plunge portions are compiled in Table 3. The complete data set can be found in the digital Appendix. Number of analyses, calculated mineral formula, and detected minor elements are summarized for each analyzed phase in Table 4.

The major element composition of pyrite is consistent throughout the 1806 zone, with Fe and S ranging between 45.22 and 46.77 wt % and 52.91 and 53.90 wt %, respectively.

TABLE 3. Microprobe Data for Selected Samples from the Up Plunge (UP) and Down Plunge (DP) of the 1806 Zone

Mineralized zone	Stringer	Semimassive sulfide						Massive sulfide			
Plunge	UP	DP									
Drill core no.	RMUG08-121	RMUG08-159						RMUG06-145			
Sample no.	29902	29934						29907			
SEM image no.	P5	P2	P5a		P7	P9	P13	P2b	P8	P10	P11	P15b
Mineral area	Py	Py	Py I	Py II	Py	Py	Py	Py	Py	Py	Py	Py
Measuring date	Apr-11	Jan-12	Jan-12	Jan-12	Jan-12	Jan-12	Jan-12	Jan-12	Jan-12	Jan-12	Jan-12	Jan-12
Pyrite and chalcopyrite												
S (wt %)	53.68	53.92	53.24	53.58	53.74	53.89	53.12	53.74	53.43	53.19	53.51	53.73
Fe	46.57	45.98	45.66	45.42	45.75	45.84	45.26	45.37	45.19	45.22	45.99	45.44
Cu (ppm)	nd	nd	nd	nd	nd	nd	550	nd	511	nd	nd	nd
Zn	nd	nd	nd	nd	3,786	516	nd	nd	nd	nd	nd	nd
Pb	nd	nd	nd	nd	nd	nd	2,803	nd	nd	nd	nd	nd
As	nd	1,557	nd	1,065	1,141	2,008	1,740	9,484	nd	nd	3,830	5,770
Sb	nd	nd	nd	nd	nd	nd	714	nd	nd	nd	nd	nd
Sn	nd	nd	nd	nd	nd	nd	nd	nd	nd	nd	nd	nd
Mo	nd	nd	nd	nd	nd	nd	1,327	nd	nd	nd	nd	nd
Co	nd	nd	nd	nd	nd	nd	nd	nd	162	nd	nd	nd
Ni	nd	nd	nd	179	nd	143	138	157	173	208	nd	234
Total	100.25	100.06	98.90	99.13	99.98	100.00	99.10	100.07	98.70	98.43	99.88	99.78

Mineralized zone	Stringer				Semimassive sulfide				Massive sulfide		
Plunge	UP				DP						
Drill core no.	RMUG08-121				RMUG08-159				RMUG08-145		
Sample no.	29902				29934				29907		
SEM image no.	P1c	P5	P14a		P2	P5a	P9	P13	P2b	P8	P10	P11
Mineral area	Ccp	Ccp	Ccp I	Ccp II	Ccp	Ccp	Ccp	Ccp	Ccp	Ccp	Ccp	Ccp
Measuring date	Apr-11	Apr-11	Apr-11	Apr-11	Jan-12	Jan-12	Jan-12	Jan-12	Jan-12	Jan-12	Jan-12	Jan-12
S (wt %)	35.35	34.83	34.92	35.02	35.01	34.98	35.45	34.94	35.12	35.27	34.92	34.84
Fe	30.49	30.38	30.48	30.48	29.86	29.93	30.21	30.05	30.27	30.10	30.20	30.09
Cu	34.93	34.72	34.94	34.57	34.24	34.26	34.28	34.44	34.36	34.24	34.39	34.23
Zn (ppm)	nd	nd	nd	699	nd	nd	nd	nd	nd	1,530	nd	nd
As	1,867	nd	nd	nd	1,200	nd	2,659	nd	nd	nd	nd	nd
Au	nd	nd	nd	nd	nd	nd	nd	nd	nd	nd	nd	nd
Ag	nd	nd	nd	nd	nd	nd	nd	nd	nd	nd	nd	nd
Sn	nd	1,212	nd	1,314	nd	nd	701	nd	nd	nd	nd	nd
Bi	nd	nd	nd	nd	nd	nd	740	nd	nd	nd	nd	nd
Mo	nd	2,099	nd	nd	nd	nd	nd	nd	nd	nd	nd	nd
Ni	nd	nd	nd	nd	nd	nd	nd	197	nd	nd	nd	nd
Total	100.96	100.26	100.33	100.27	99.23	99.16	100.34	99.45	99.75	99.76	99.51	99.16

Table 3 (*Cont.*) Pyrite and Chalcopyrite

Mineralized zone	Massive sulfide								Silicified rhyolite	
Plunge	UP								UP	
Drill core no.	RMUG08-142					RMUG08-123				RMUG08-140
Sample no.	29778					36512				29783
SEM image no.	P3a	P10b	P11	P16a-3		P3	P5b		P12	P7
Mineral area	Py	Py	Py	Py N rim	Py core	Py	Py I	Py II	Py	Py
Measuring date	Apr-11	Apr-11	Apr-11	Apr-11	Apr-11	Apr-11	Apr-11	Apr-11	Apr-11	Apr-11
S (wt %)	53.63	53.66	53.77	53.41	53.23	53.47	53.18	53.62	53.34	53.90
Fe	46.76	46.44	46.65	46.19	46.12	46.68	46.68	46.11	46.77	46.55
Cu (ppm)	nd	859	545	nd	nd	nd	nd	nd	nd	nd
Zn	nd	nd	nd	nd	nd	nd	nd	nd	nd	nd
Pb	nd	nd	nd	nd	nd	nd	nd	nd	nd	nd
As	nd	3,274	nd	nd	4,607	1,678	nd	4,047	nd	8,240
Sb	nd	nd	nd	nd	nd	nd	nd	nd	nd	nd
Sn	nd	1,083	1,339	nd	nd	nd	1,032	nd	nd	nd
Mo	nd	nd	nd	nd	nd	nd	nd	nd	nd	nd
Co	nd	nd	nd	nd	nd	nd	nd	nd	nd	nd
Ni	nd	nd	nd	295	nd	475	296	741	nd	nd
Total	100.39	100.63	100.60	99.63	99.82	100.36	99.99	100.21	100.11	101.27

Mineralized zone	Massive sulfide								Silicified rhyolite		
Plunge	DP	UP							UP		
Drill core no.	RMUG08-145	RMUG08-142				RMUG08-123			RMUG08-140		
Sample no.	29907	29778				36512			29783		
SEM image no.	P15b	P3a	P11	P16a-3		P3	P5b	P1		P5	P6	P7
Mineral area	Ccp	Ccp	Ccp	Ccp	Ccp	Ccp	Ccp	Ccp core	Ccp SW rim	Ccp	Ccp	Ccp
Measuring date	Jan-12	Apr-11	Apr-11	Apr-11	Apr-11	Apr-11	Apr-11	Apr-11	Apr-11	Apr-11	Apr-11	Apr-11
S (wt %)	35.23	35.09	34.85	35.01	33.76	34.98	34.91	34.95	34.98	35.00	34.97	35.17
Fe	29.97	30.25	30.14	30.50	28.25	30.49	30.36	30.38	30.43	30.45	30.57	30.31
Cu	34.49	34.43	34.66	34.69	32.76	34.50	34.40	34.61	34.13	34.53	34.45	34.96
Zn (ppm)	nd	nd	1,011	nd	nd	nd	nd	nd	nd	nd	nd	682
As	nd	nd	nd	nd	nd	nd	nd	nd	nd	nd	nd	nd
Au	1,074	nd	nd	nd	nd	nd	nd	nd	nd	nd	nd	nd
Ag	nd	nd	nd	1,756	*4.14*	nd	1,522	3,433	4,394	nd	nd	nd
Sn	nd	2,063	nd	960	nd	2,326	1,160	nd	nd	nd	nd	nd
Bi	nd	nd	nd	nd	nd	nd	nd	nd	nd	nd	nd	nd
Mo	nd	nd	nd	nd	nd	nd	nd	nd	nd	nd	nd	1,410
Ni	nd	nd	nd	nd	nd	nd	nd	nd	nd	nd	nd	nd
Total	99.80	99.98	99.75	100.47	98.91	100.20	99.94	100.27	99.98	99.98	100.00	100.65

TABLE 3 (*Cont.*) Sphalerite and Arsenopyrite

Mineralized zone	Stringer			Semimassive sulfide				Massive sulfide				
Plunge	UP			DP				UP				
Drill core no.	RMUG08-121			RMUG08-159		RMUG08-145	RMUG08-142	RMUG08-123				
Sample no.	29902			29934		29907	29778	36512				
SEM image no.	P1c	P14a		P5a	P7	P2b	P11	P3	P5b		P7b	P12
Mineral	Sp	Sp I	Sp II	Sp	Sp	Sp	Sp	Sp	Sp I	Sp II	Sp	Sp
Measuring date	Apr-11	Apr-11	Apr-11	Jan-12	Jan-12	Jan-12	Apr-11	Apr-11	Apr-11	Apr-11	Apr-11	Apr-11
S (wt %)	33.41	33.33	33.29	33.19	33.18	33.03	32.98	33.08	33.02	33.25	32.93	32.69
Fe	5.45	4.79	4.78	1.70	1.12	8.56	1.80	9.00	9.37	8.41	9.19	6.12
Zn	60.60	62.02	61.24	64.09	65.10	57.16	64.32	57.11	55.76	57.36	56.59	60.20
Cu (ppm)	2,162	709	1,585	2,106	926	1,656	4,877	nd	1,802	nd	nd	nd
As	*1.14*	nd	nd	nd	nd	nd	nd	nd	nd	nd	nd	nd
Bi	nd	nd	nd	nd	1,116	nd	nd	nd	nd	nd	nd	nd
Hg	nd	2,844	2,239	nd	nd	nd	nd	3,257	3,234	3,145	3,145	2,799
Mn	756	1,706	1,081	2,472	2,190	534	1,177	1,193	1,737	1,062	1,162	1,220
Total	100.89	100.67	99.95	99.45	99.82	98.97	99.70	99.64	98.83	99.45	99.14	99.41

Mineralized zone	Stringer					Semimassive sulfide			Massive sulfide			
Plunge	UP					DP						
Drill core no.	RMUG08-121					RMUG08-159			RMUG08-145			
Sample no.	29902					29934			29907			
SEM image no.	P1c		P5		P14a	P2	P5a	P9	P2b	P8	P11	
Mineral area	Asp I	Asp II	Asp I	Asp II	Asp	Asp	Asp	Asp	Asp	Asp	Asp left	Asp right
Measuring date	Apr-11	Apr-11	Apr-11	Apr-11	Apr-11	Jan-12	Jan-12	Jan-12	Jan-12	Jan-12	Jan-12	Jan-12
S (wt %)	21.30	21.46	21.86	21.61	21.45	20.97	21.54	21.73	20.91	21.69	20.52	19.50
Fe	34.55	34.76	34.98	34.65	34.87	34.67	34.69	34.71	34.38	34.49	34.17	34.01
As	43.61	43.54	43.56	43.88	43.80	45.04	44.26	44.80	44.24	43.99	45.12	46.68
Cu (ppm)	626	709	536	nd	2,024	703	463	nd	nd	nd	531	nd
Zn	*1.07*	nd	nd	nd	nd	nd	nd	nd	nd	nd	nd	nd
Au	nd	nd	1485	nd	nd	nd	nd	nd	nd	nd	nd	nd
Sb	nd	nd	nd	nd	nd	nd	nd	nd	nd	nd	nd	2,441
Sn	nd	nd	nd	nd	nd	nd	nd	nd	nd	nd	nd	nd
Te	nd	nd	nd	nd	2,543	825	nd	nd	nd	nd	nd	nd
Bi	nd	nd	nd	nd	nd	nd	nd	nd	nd	nd	1,296	nd
Mo	nd	nd	nd	nd	nd	nd	nd	nd	nd	nd	nd	nd
Ni	2,971	182	673	387	533	nd	1,546	904	916	1,618	372	nd
Total	100.89	99.84	100.66	100.18	100.62	100.83	100.68	101.33	99.63	100.33	100.04	100.43

TABLE 3 (*Cont.*) Sphalerite and Arsenopyrite

Mineralized zone	Silicified rhyolite	
Plunge	UP	
Drill core no.	RMUG08-140	
Sample no.	29783	
SEM image no.	P6	P16a-3
Mineral	Sp	Sp
Measuring date	Apr-11	Apr-11
S (wt %)	32.79	33.09
Fe	9.71	1.94
Zn	55.79	64.86
Cu (ppm)	nd	937
As	nd	nd
Bi	nd	nd
Hg	nd	nd
Mn	795	1,559
Total	98.38	100.15

Mineralized zone	Massive sulfide						Silicified rhyolite			
Plunge	DP	UP					UP			
Drill core no.	RMUG08-145	RMUG08-142				RMUG08-123	RMUG08-140			
Sample no.	29907	29778				36512	29783			
SEM image no.	P15b	P10b			P11	P5b	P1	P7		
Mineral area	Asp	Asp NE rim	Asp core	Asp SW rim	Asp	Asp	Asp	Asp NW rim	Asp core	Asp SE rim
Measuring date	Jan-12	Apr-11	Apr-11	Apr-11	Apr-11	Apr-11	Apr-11	Apr-11	Apr-11	Apr-11
S (wt %)	21.68	21.10	21.79	21.17	20.83	19.81	22.00	21.44	21.37	21.57
Fe	34.66	34.79	34.94	34.74	34.52	34.15	34.48	34.78	34.82	34.90
As	43.82	44.02	43.38	43.30	42.60	45.29	42.32	43.94	43.61	43.24
Cu (ppm)	nd	nd	nd	nd	4906	nd	1506	nd	nd	nd
Zn	nd	nd	nd	nd	661	nd	nd	nd	nd	nd
Au	nd	nd	nd	nd	nd	nd	nd	nd	nd	nd
Sb	nd	nd	nd	nd	nd	2377	nd	nd	nd	nd
Sn	nd	nd	nd	nd	nd	nd	nd	1,131	nd	nd
Te	nd	nd	nd	nd	nd	nd	1419	nd	nd	nd
Bi	nd	nd	nd	nd	nd	nd	nd	nd	nd	nd
Mo	nd	3,532	4,711	4,603	nd	4,123	nd	nd	nd	nd
Ni	1,384	1,118	1,238	289	543	nd	1,057	737	921	1,110
Total	100.29	100.37	100.71	99.70	98.56	99.90	99.20	100.35	99.89	99.82

TABLE 3 (*Cont.*) Tennantite-Tetrahedrite and Mercurian Electrum

Mineralized zone	Stringer			Semimassive sulfide								
Plunge	UP			DP								
Drill core no.	RMUG08-121			RMUG08-159								
Sample no.	29902			29934								
SEM image no.	P14a			P2				P7	P9	P13		
Mineral area	Tet N rim	Tet core	Tet S rim	Tet I	Tet II core	Tet II rim-a	Tet II rim-b	Tet I	Tet	Tet rim-a	Tet rim-b	Tet core
Measuring date	Apr-11	Apr-11	Apr-11	Jan-12	Jan-12	Jan-12	Jan-12	Jan-12	Jan-12	Jan-12	Jan-12	Jan-12
S (wt %)	24.33	24.53	24.64	24.71	24.45	24.37	24.36	23.86	24.18	24.25	24.15	24.25
Fe	3.57	3.69	3.47	2.88	2.78	3.13	2.54	2.90	1.99	3.01	4.19	2.69
Cu	33.49	32.61	33.57	34.88	34.18	33.96	34.23	32.88	34.08	32.06	31.91	32.82
Zn	3.51	3.22	3.51	4.59	4.61	4.30	4.94	4.34	5.49	4.80	4.63	4.86
As	1.30	2.05	1.64	3.47	2.27	2.78	1.94	1.32	1.25	1.94	1.84	2.07
Sb	26.12	25.57	26.05	24.08	25.91	24.84	26.51	27.33	27.69	26.37	25.78	26.35
Ag	6.05	7.30	6.07	4.94	5.26	5.83	5.29	6.41	4.68	7.67	7.14	6.73
Pb (ppm)	nd	nd	nd	nd	1,642	nd	nd	nd	nd	nd	nd	nd
Sn	nd	nd	nd	nd	nd	nd	743	nd	nd	nd	nd	nd
Bi	nd	nd	nd	1,700	nd	nd	nd	nd	nd	nd	nd	871
Hg	1,994	nd	nd	nd	nd	nd	nd	nd	nd	nd	nd	nd
Mn	nd	nd	nd	nd	nd	nd	nd	nd	nd	nd	nd	nd
Total	98.58	98.98	98.95	99.72	99.63	99.21	99.89	99.04	99.35	100.11	99.63	99.86
Sb/(Sb + As)*	0.92	0.88	0.91	0.81	0.88	0.85	0.89	0.93	0.93	0.89	0.90	0.89
Zn/(Zn + Fe)*	0.46	0.43	0.46	0.58	0.59	0.54	0.62	0.56	0.70	0.58	0.49	0.61

Mineralized zone	Stringer					Massive sulfide		Silicified rhyolite				
Plunge	UP					DP	UP	UP				
Drill core no.	RMUG08-21					RMUG08-159	RMUG08-142	RMUG08-140				
Sample no.	29902					29934	29778	29783				
SEM image no.	P14a					P5a	P16a-3	P1			P5	
Mineral area	El core	El core-1	El E rim	El W rim I	El W rim II	El	El	El I core	El I E rim	El II	El I	El II
Measuring date	Apr-11	Apr-11	Apr-11	Apr-11	Apr-11	Jan-12	Apr-11	Apr-11	Apr-11	Apr-11	Apr-11	Apr-11
Au (wt %)	41.34	44.96	59.31	37.43	38.34	43.48	13.87	46.61	41.18	38.30	39.18	41.73
Ag	39.82	37.96	30.45	44.52	45.45	36.88	67.35	36.70	43.53	46.97	43.09	43.97
Hg	17.90	17.02	11.30	17.20	14.50	20.57	16.97	17.15	15.77	13.05	15.53	14.16
S (ppm)	939	1,222	1,393	330	1,017	190	6,525	914	3,112	9,666	5,961	4,987
Fe	535	nd	366	697	304	642	4,722	526	1,637	5,423	2,752	4,745
Cu	nd	nd	nd	nd	nd	776	1,212	nd	nd	nd	nd	nd
Sb	nd	nd	nd	693	2,303	nd	nd	nd	nd	nd	nd	nd
Co	nd	173	nd	nd	nd	151	nd	157	nd	nd	nd	nd
Ni	nd	nd	nd	nd	nd	nd	210	nd	nd	nd	nd	nd
Total	99.20	100.09	101.24	99.32	98.65	101.11	99.45	100.62	100.98	99.82	98.67	100.84
Au/Ag	1.04	1.18	1.95	0.84	0.84	1.18	0.21	1.27	0.95	0.82	0.91	0.95

TABLE 3 (*Cont.*) Tennantite-Tetrahedrite, Mercurian Electrum, and Ag phases

Mineralized zone	Massive sulfide			
Plunge	UP			
Drill core no.	RMUG08-142			
Sample no.	29778			
SEM image no.	P3a		P11	
Mineral area	Ten I	Ten II	Ten-Tet W part	Ten-Tet E part
Measuring date	Apr-11	Apr-11	Apr-11	Apr-11
S (wt %)	28.52	28.14	25.03	25.70
Fe	4.99	5.30	2.24	2.38
Cu	42.15	41.29	30.10	32.84
Zn	2.90	3.24	5.28	5.33
As	19.05	18.14	6.28	8.08
Sb	2.52	3.03	17.44	15.83
Ag	0.514	0.550	12.51	8.78
Pb (ppm)	nd	nd	nd	nd
Sn	nd	nd	nd	nd
Bi	nd	nd	nd	nd
Hg	nd	nd	nd	nd
Mn	227	nd	nd	nd
Total	100.67	99.69	98.88	98.96
Sb/(Sb + As)*	0.08	0.09	0.63	0.55
Zn/(Zn + Fe)*	0.33	0.34	0.67	0.66

Mineralized zone	Massive sulfide			Silicified rhyolite
Plunge	UP			UP
Drill core no.	RMUG08-123			RMUG08-140
Sample no.	36512			29783
SEM image no.	P5b		P7b	P1
Mineral area	Hg-Stp	AgCuFeS	Pyr	Mia
Measuring date	Apr-11	Apr-11	Apr-11	Apr-11
S (wt %)	15.18	27.31	17.77	21.86
Ag	57.30	27.20	58.76	35.90
Fe	0.253	22.24	nd	0.040
Cu	0.391	22.89	nd	0.191
As	1.17	nd	0.104	nd
Sb	11.32	nd	21.87	41.13
Hg	12.74	nd	nd	nd
Pb (ppm)	nd	nd	6,006	nd
Au	3,502	nd	nd	nd
Mo	2,256	nd	nd	nd
Co	nd	nd	159	nd
Total	98.93	99.86	100.07	99.13

Mineralized zone	Silicified rhyolite		
Plunge	UP		
Drill core no.	RMUG08-140		
Sample no.	29783		
SEM image no.	P6		
Mineral area	El I	El II	El III
Measuring date	Apr-11	Apr-11	Apr-11
Au (wt %)	37.69	41.24	39.75
Ag	47.70	44.64	44.72
Hg	13.76	13.50	13.78
S (ppm)	1,566	1,823	2,473
Fe	601	1,038	1,962
Cu	nd	nd	nd
Sb	761	nd	961
Co	nd	163	nd
Ni	nd	174	nd
Total	99.44	99.70	98.79
Au/Ag	0.79	0.92	0.89

Note: Italics indicate values in wt % rather than ppm

Abbreviations: * = molecular proportion, AgCuFeS = unnamed AgCuFeS phase, Asp = arsenopyrite, Ccp = chalcopyrite, El = (mercurian) electrum, Hg-Stp = mercurian stephanite, Mia = miargyrite, nd = not detected, Py = pyrite, Pyr = pyrargyrite, Sp = sphalerite, Ten = tennantite, Ten-Tet = tennantite-tetrahedrite, Tet = tetrahedrite

TABLE 4. Summary of Microprobe Analyses—Mineral Phases, Their Calculated Mineral Formulas, and Detected Minor Elements

Mineral	Pyrite	Chalcopyrite	Unknown phase	Sphalerite	Galena
Number of analyses	42	58	3	30	30
Calculated mineral formula	$Fe_{0.97-1.02}S_2$	$Cu_{0.97-1.01}Fe_{0.94-1.02}S_2$	N/A	Low-Fe Sp: $(Zn_{0.94-0.97}, Fe_{0.02-0.05})S$ Med-Fe Sp: $(Zn_{0.87-0.91}, Fe_{0.08-0.11})S$ High-Fe Sp: $(Zn_{0.81-0.85}, Fe_{0.15-0.18})S$	$Pb_{0.95-1.08}S$
Minor elements (<1 wt %)	As, Cu, Zn, Pb, Sb, Sn, Hg, Mo, Ni	Zn, As, Au, Ag, Sn, Te, Bi, Mo, Ni	As, Hg	Cu, As, Ag, Sn, Hg, Bi, Mn, Ni	Fe, Cu, As, Zn, Ag, Sb, Te, Mn
Comments			Reaction between Ccp and El; low totals (78–79 wt %); only in UP	Low- and high-Fe sphalerites occur from UP to DP; mid-Fe sphalerites are only in UP	

Mineral	Pyrrhotite	Arsenopyrite	Tennantite-tetrahedrite
Number of analyses	12	48	53
Calculated mineral formula	$Fe_{1-x}S$ (x = 0.12-0.14)	$Fe_{0.83-1.00}As_{0.75-1.02}S$	Ten: $(Cu_{9.63-10.63}, Ag_{0.04-0.14})_{\Sigma=9.70-10.72}(Fe_{1.23-1.60}, Zn_{0.42-0.74})_{\Sigma=1.96-2.31}(As_{3.02-3.90}, Sb_{0.16-0.96})_{\Sigma=3.81-4.08}S_{13}$ Ten-Tet: $(Cu_{6.18-9.91}, Ag_{0.14-3.64})_{\Sigma=9.62-10.08}(Fe_{0.67-1.86}, Zn_{0.27-1.34})_{\Sigma=1.94-2.11}(As_{1.38-2.76}, Sb_{1.22-2.81})_{\Sigma=3.78-4.19}S_{13}$ Tet: $(Cu_{4.60-9.64}, Ag_{0.36-5.39})_{\Sigma=9.50-10.63}(Fe_{0.61-2.30}, Zn_{0.09-1.45})_{\Sigma=1.96-2.52}(As_{0-0.88}, Sb_{3.26-4.37})_{\Sigma=3.97-4.52}S_{13}$
Minor elements (<1 wt %)	Cu, Zn, Pb, As, Sn, Mo, Ni	Cu, Zn, Pb, Au, Ag, Sb, Sn, Te, Bi, Mo, Mn, Ni	Pb, Bi, Sn, Te, Hg, Mn
Comments	Sn-bearing Po in UP and adjacent to El		Some Ag-rich tetrahedrites of freibergite composition

Mineral	Ag phases	Mercurian electrum	Boulangerite	Stannite	Molybdenite
Number of analyses	5 (Mia: 2; Pyr: 1; Hg-Stp: 1; unnamed AgCuFeS phase: 1)	24	3	4	1
Calculated mineral formula	Mia: $Ag_{0.98-1.07}Sb_{0.96-0.99}S_2$ Pyr: $Ag_{2.95}Sb_{0.97}S_3$ Hg-Stp: $(Ag_{4.49}, Hg_{0.54})_{\Sigma=5.03}(Sb_{0.79}, As_{0.13})_{\Sigma=0.92}S_4$ Unnamed AgCuFe S phase: N/A	N/A	$Pb_{5.85-6.27}(Sb_{3.35-3.49}, Cu_{0.49-1.06})_{\Sigma=3.84-4.52}S_{11}$	$Cu_{1.91-1.95}(Fe_{0.92-0.96}, Zn_{0.13-0.18})_{\Sigma=1.07-1.12}Sn_{1.00-1.01}S_4$	$(Mo_{1.02}, Fe_{0.03})_{\Sigma=1.05}S_2$
Minor elements (<1 wt %)	Mia: Cu, Fe, As, Hg Pyr: As, Pb, Co Hg-Stp: Fe, Cu, Mo, Au unnamed AgCuFeS phase: N/A	S, Fe, Cu, Zn, Pb, As, Sb, Bi, Co, Ni	Fe, Zn, Ag, Sn	As, Ni, Mn	Cu, Au, Te
Comments		High Hg content (7.93 to 20.97 wt %)	More of falkmanite composition than boulangerite	Restricted to UP portion of semimassive to massive sulfide lens	

Mineral	Cassiterite	Magnetite
Number of analyses	2	9
Calculated mineral formula	$Sn_{0.97-0.98}O_2$	$Fe_{2.74-2.90}O_4$
Minor elements (<1 wt %)	Cu, As, Fe	S, Cu, Zn, Mn
Comments	Only in DP	Only in DP

Abbreviations: AgCuFeS = unnamed AgCuFeS phase, DP = down plunge, El = (mercurian) electrum, Hg-Stp = mercurian stephanite, Mia = miargyrite, Pyr = pyrargyrire, Sp = sphalerite, Ten = tennantite, Ten-Tet = tennantite-tetrahedrite, Tet = tetrahedrite, UP = up plunge

All pyrite analyses have near-stoichiometric compositions with some grains showing As substitution ranging from 1,065 to 9,484 ppm (Fig. 11a). The arsenian pyrite grains do not show any spatial association with either As-rich phases (e.g., arsenopyrite, tennantite) or electrum. Most chalcopyrite analyses are near stoichiometric with Cu, Fe, and S ranging between 32.76 and 35.55 wt %, 28.25 and 30.77 wt %, and 33.76 and 36.13 wt %, respectively.

Sphalerite grains from all mineralized zones within the 1806 zone have a wide range of Fe content between 1.12 and 10.16 wt %, with Zn and S concentrations ranging between 54.75 and 65.28 wt % and 32.33 and 33.52 wt %, respectively. Sphalerite is near stoichiometric with Fe substituting on the Zn site (e.g., Vaughan and Craig, 1978; Di Benedetto et al., 2005; Wright, 2009). Based on the Fe content, three different populations can be distinguished (Fig. 11b): (1) low-Fe sphalerites have Fe contents of 1.12 to 2.94 wt % with Zn contents of 65.10 to 63.24 wt %, (2) medium-Fe sphalerites have Fe contents of 4.78 to 6.36 wt % at Zn values of 61.24 to 58.12 wt %, and (3) high-Fe sphalerites have concentrations of 8.41 to 10.16 wt % Fe at 57.36 to 54.83 wt %. Low-Fe and high-Fe sphalerites occur from the down-plunge area to the

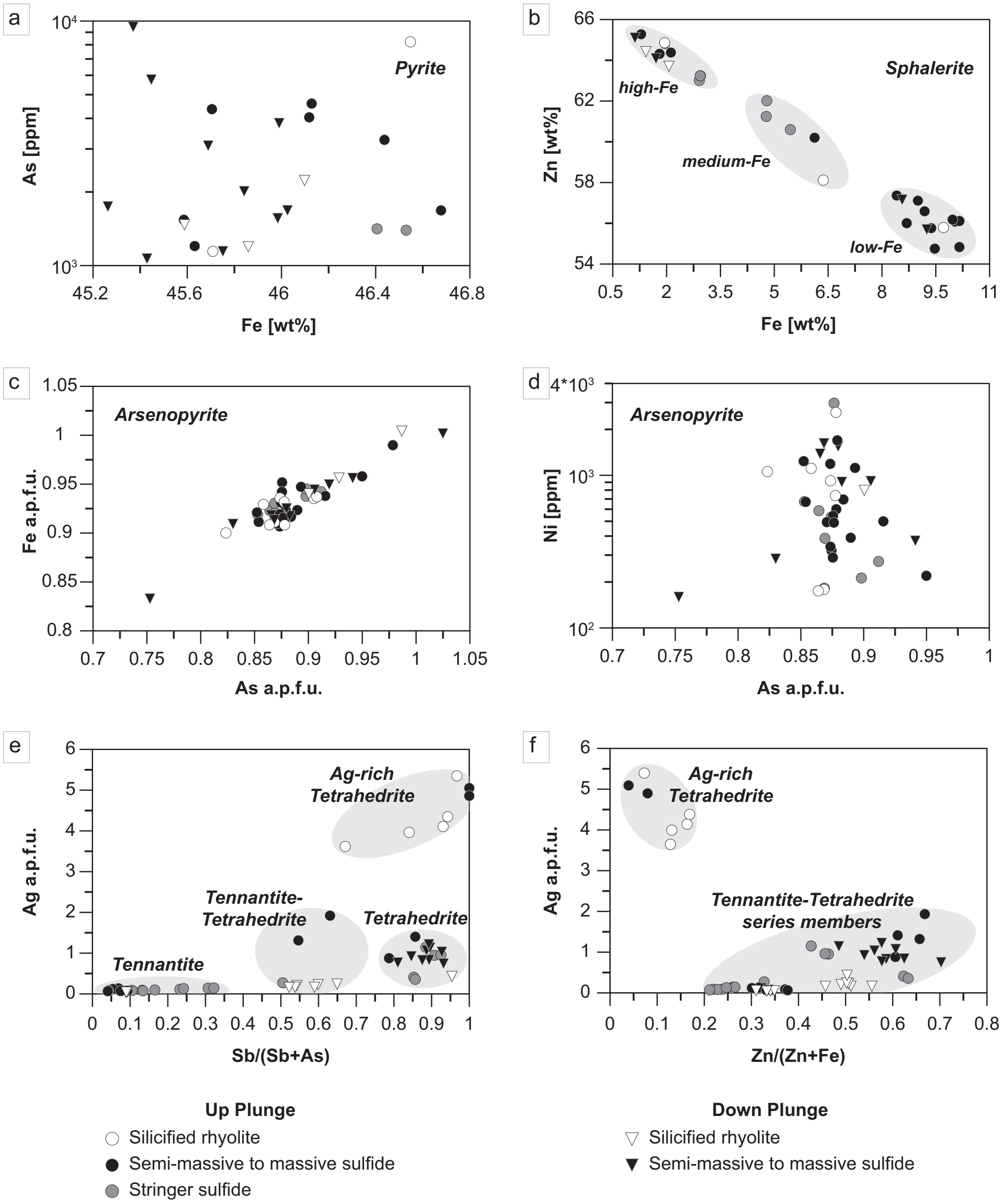

FIG. 11. Compositional plots for various sulfide and sulfosalt phases based on EPMA analyses. (a) Fe vs. As in pyrite. (b) Fe vs. Zn in sphalerite; shaded areas highlight three distinct Fe populations within sphalerite. (c, d) Compositional variations in arsenopyrite. (e, f) Compositional variations in members of the tennantite-tetrahedrite series. See text for details.

up-plunge area, whereas medium-Fe sphalerites are detected only in the up-plunge portion of the 1806 zone (Fig. 11b).

Analyzed galena grains have Pb and S content of 83.94 to 87.55 wt % and of 12.27 to 13.90 wt %, respectively, and have a minor excess of Pb in their mineral formula.

Pyrrhotite grains were measured in the semimassive to massive sulfide horizon and in the silicified horizon in the 1806 zone. Their major composition is homogeneous with Fe and S ranging between 59.63 and 60.69 wt % and 38.85 and 40.14 wt %, respectively.

Arsenopyrite analyses from throughout the 1806 zone range in Fe, As, and S from 33.58 to 34.98 wt %, from 41.69 to 46.68 wt %, and from 19.50 to 23.71 wt %, respectively. They are nonstochiometric with deficiencies in both Fe and As (Fig. 11c). Furthermore, the analyzed arsenopyrite grains are more deficient in As than in Fe (Fig. 11c). Most arsenopyrite data show a wide abundance of minor elements including variable enrichments in transition metals (Ni, Mn) and the epithermal suite of elements (Bi, Sb, Te), including Au and Ag; however, the measured concentration of these traces cannot equalize the deficiency in either Fe or As in the arsenopyrite. The most abundant minor element in arsenopyrite is Ni; however, Ni does not show a clear correlation to any of the major phases or locations within the 1806 zone (Fig. 11d).

Tennantite-tetrahedrite is one of the most complex solid solution series within the heterogeneous sulfosalt group (Moëlo et al., 2008). Major and minor components include Cu (15.29–44.46 wt %), Ag (0.29–29.27 wt %), Fe (1.99–6.56 wt %), Zn (0.31–5.49 wt %), As (0–19.25 wt %), Sb (1.33–29.06 wt %), and S (20.99–28.52 wt %). Among the analyzed species, end members of tennantite ($Sb/(Sb + As) < 0.35$) and tetrahedrite ($Sb/(Sb + As) > 0.7$) are present, in addition to solid solutions between both end members (Fig. 11e). The Ag content is highly variable within tennantite-tetrahedrite, with all tennantite having Ag < 0.2 Ag apfu, and there is a general increase in Ag content with increasing Sb concentration (i.e., from tennantite-tetrahedrite to tetrahedrite; Fig. 11e). The highest Ag contents are found in seven tetrahedrite analyses from the up-plunge portion of the 1806 zone (Fig. 11e, f). They have more than 3.5 Ag apfu and are in this paper referred to as Ag-rich tetrahedrite, also known as freibergite. Tennantite-tetrahedrite ranges from Zn poor to Zn rich ($0.2 \leq Zn/(Zn + Fe) \leq 0.7$) and Ag increases with increasing $Zn/(Zn + Fe)$. In contrast, Ag-rich tetrahedrite is Zn poor ($Zn/(Zn + Fe) < 0.2$) and the Ag content decreases with increasing $Zn/(Zn + Fe)$ (Fig. 11e). Members of the tennantite-tetrahedrite series are both stoichiometric and nonstoichiometric.

Various Ag phases (i.e., miargyrite, pyrargyrite, mercurian stephanite, unnamed AgCuFeS phase) from the up-plunge portion of the deposit were analyzed from the 1806 zone. They are spatially associated with and occur in close proximity to electrum (Figs. 8g, j, m, 10g-j), arsenopyrite (Figs. 8g, j, k, m, 10g-j), and/or sulfosalts (Figs. 8g, j, k, m, 10g-j). Miargyrite (Fig. 8m) has concentrations for Ag, Sb, and S between 35.90 and 37.52 wt %, 38.01 and 41.13 wt %, and 20.86 and 21.86 wt %, respectively; one miargyrite analysis reported elevated Zn (1.19 wt %) and Au (2.43 wt %), most likely due to contamination from adjacent sphalerite and electrum, respectively. Pyrargyrite (Fig. 8k) has 58.76 wt % Ag, 21.87 wt % Sb, and 17.77 wt % S. The calculated formula shows a weak deficiency on both the Ag and Sb site. Mercurian stephanite contains 57.30 wt % Ag, 11.32 wt % Sb, 15.18 wt % S, 12.74 wt % Hg, and 1.17 wt % As. An unnamed AgCuFeS phase is found next to mercurian stephanite (Figs. 8j, 10g-j), containing Ag (27.20 wt %), Cu (22.89 wt %), Fe (22.24 wt %), and S (27.31 wt %). Mineral formula calculations based on different S apfu were unsuccessful.

The term "electrum" (AuAg) is used in this paper for Au-Ag alloys with >10 wt % Au, and all analyzed electrum minerals have elevated Hg. Most of the 24 available electrum analyses are from the up-plunge portion of the 1806 zone. Gold, Ag, and Hg concentrations in electrum range between 13.87 and 61.99 wt %, 30.29 and 67.35 wt %, and 7.93 and 20.57 wt %, respectively (Fig. 12a). Most samples have >30 wt % Au and Au/Ag ratios that range from 0.21 to 2.05 (Fig. 12b). All samples from the stringer zone and the silicified cap horizon, except one, show an Au/Ag ratio of about 1 ($0.79 \leq Au/Ag \leq 1.27$) and the Hg concentration increases with increasing Au/Ag ratio (Fig. 12b). In contrast, samples from the semimassive to massive sulfide horizon have a much wider range in Au/Ag ratio (0.21–2.05) and, in general, Hg concentration

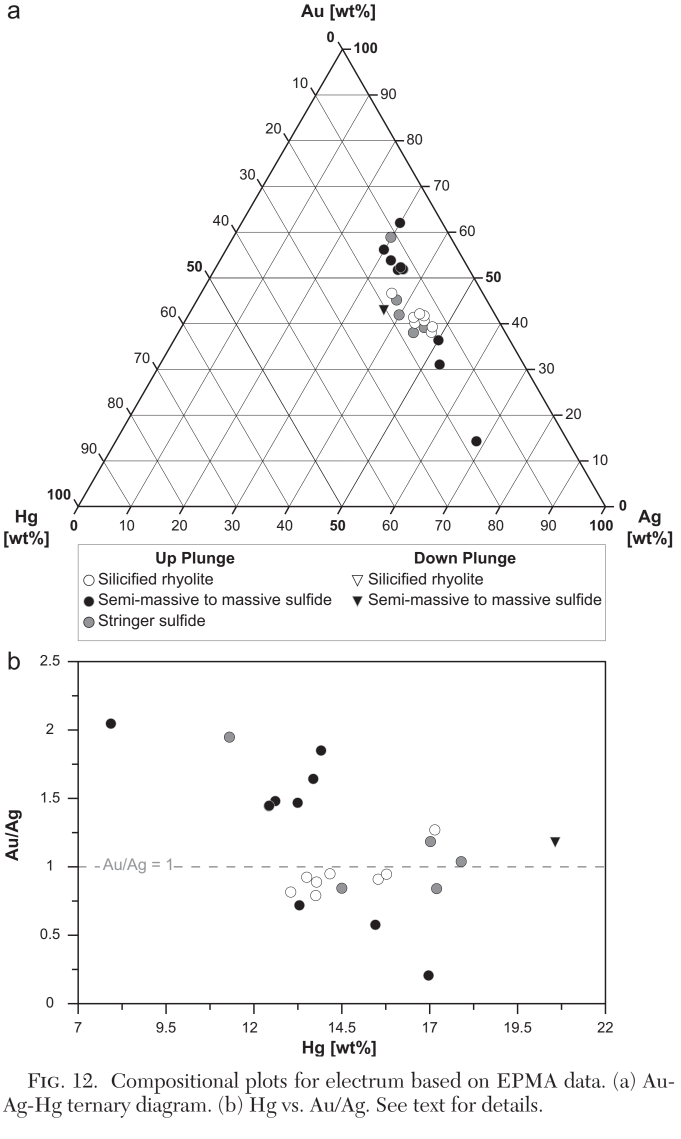

FIG. 12. Compositional plots for electrum based on EPMA data. (a) Au-Ag-Hg ternary diagram. (b) Hg vs. Au/Ag. See text for details.

decreases with increasing Au/Ag ratio (Fig. 12b). Some of the mercurian electrum grains were large enough to analyze the rim and core areas. Data from these grains reveal that the rim is enriched in Ag compared to the core (Fig. 10d), whereas the core is enriched in Au (Fig. 10c). Mercury does not show a uniform trend with Au or Ag (Fig. 10c-e).

Boulangerite, stannite, cassiterite, and magnetite were also analyzed by EPMA. Both boulangerite (falkmanite composition) and magnetite are nonstoichiometric, whereas molybdenite and cassiterite are broadly stoichiometric.

Discussion

Syngenetic vs. synorogenic precious metal emplacement

The origin of precious metal enrichment in ancient VMS deposits is often contentious, particularly for deformed deposits in ancient belts, where primary characteristics might have been obscured and altered by younger events. These events can be of different origin. For instance, some workers have argued that Au enrichment in some Au-rich VMS deposits was due to later orogenic overprinting and Au introduction by metamorphic fluids (e.g., Bousquet 1 and Dumagami: Tourigny et al., 1989; Marquis et al., 1990). In contrast, in other deposits, it has been argued that the enrichment in precious metals was due to epithermal (magmatic) overprinting or formation as shallow-water magmatic-hydrothermal systems (e.g., Eskay Creek: Roth et al., 1999; Boliden: Bergman-Weihed et al., 1996; Wagner and Jonsson, 2001; Mercier-Langevin et al., 2013). Gold enrichment in the Rambler camp is debated as well, in large part because the deposit is polydeformed and metamorphosed, and occurs proximal to deposits that are typical orogenic Au deposits (e.g., Deer Cove: Patey and Wilton, 1993; Stog'er Tight: Ramezani et al., 2000).

The specific characteristics of the 1806 zone of the Ming mine documented here illustrate that, despite significant deformation and metamorphic overprint, the precious metal mineralization is syngenetic and results from a primary or synvolcanic hydrothermal fluid. Moreover, ore mineralogy and mineral chemistry indicate a possible magmatic input into the ore-forming hydrothermal system.

Architecture: The overall architecture of the 1806 zone is typical of most VMS deposits, with a discordant (although transposed) stringer and footwall alteration zone underlying concordant or stratabound semimassive to massive sulfides. The silicified and mineralized horizon located at the footwall-hanging wall contact (Fig. 4) contains remnants of the host rock (i.e., relict clasts) and strongly resembles the silica- and chlorite-altered footwall Rambler rhyolite. While there are numerous potential origins for this silicified horizon, which are not focus of this paper, its texture and aspect as well as the absence of carbonates in both the horizon and its immediate wall rocks preclude the possibility that this horizon could be a late, orogenic quartz vein superimposed on the VMS system. Such orogenic quartz veins have clear, quasiuniversal features that make them relatively easy to identify (e.g., Groves et al., 1998; Bierlein and Crowe, 2000), and the orogenic vein systems on the Baie Verte Peninsula are no exception (e.g., Evans and Wells, 1998; Ramezani et al., 2000). The semimassive to massive sulfide lens of the 1806 zone is separated from the other mineralized horizons (1807 zone, Ming South, Ming North, Lower Footwall) and the previously mined horizon (Fig. 3) by mafic dikes (Pilote and Piercey, 2013). Despite the unknown age and relation of these mafic dikes relative to the massive sulfide deposition (Pilote and Piercey, 2013), an active role of these dikes in the precious metal deposition is excluded, because sulfide mineralization is sparse in these dikes and restricted to random disseminated pyrite cubes on the sharp contacts to the mineralized lithounits (i.e., Rambler rhyolite, semimassive and massive lens, silicified rhyolite). Furthermore, there are no enrichments in precious metals or precious metal minerals proximal to dike contacts. The contacts between mineralized footwall-sulfide lens–silicified rhyolite are sharp, but not tectonically induced. Moreover, all sulfide zones at the Ming mine are trending northeast with a plunge of 30° to 35°, which is similar to the dip of the Rambler rhyolite (Tuach and Kennedy, 1978), indicating the predeformational origin for the various sulfide lenses at the Ming mine, in general, and of the 1806 zone, specifically.

Alteration: An assemblage of sericite-quartz ± green mica with sporadic biotite-chlorite dominates the alteration in the footwall Rambler rhyolite. Although advanced argillic or aluminous alteration, characteristic of high sulfidation epithermal deposits, is associated with a number of Au-rich VMS deposits (Sillitoe et al., 1996; Hannington et al., 1999; Huston, 2000; Dubé et al., 2007a; Mercier-Langevin et al., 2011), it is not well developed at the 1806 zone. The sericitic alteration of the footwall of the 1806 zone is rather common for base metal VMS deposits (e.g., Franklin et al., 1981) and in lower sulfidation epithermal Au deposits (Bierlein and Crowe, 2000; Hedenquist et al., 2000). Although the 1806 zone does not have features characteristic of subaerial epithermal deposits (e.g., cavity-filled veins or veinlet stockworks, bladed calcite, and native gold; Hedenquist et al., 2000), the sulfide mineral assemblage at the 1806 zone is typical intermediate sulfidation epithermal assemblage (Figs. 7, 8; Sillitoe and Hedenquist, 2003, and references therein).

Metal zoning: Metal zoning is well documented from base metal and Au-rich VMS deposits and is caused by changing fluid conditions (T, pH, f_{O_2}) over the lifespan of the hydrothermal system (e.g., Large, 1977, 1992; Huston and Large, 1989; Ohmoto, 1996; Poulsen and Hannington, 1996; Hannington et al., 1999). Orogenic Au deposits lack this feature (Goldfarb et al., 2005). At the 1806 zone, base metal and precious metal zoning is observed from the down-plunge portion (high-grade Cu zone, low-grade Zn, Au, and Ag) to the up-plunge part (high-grade Zn, Pb, and precious metal contents, lower-grade Cu values; Fig. 9). In context of metal associations, the 1806 zone shows an Au-Zn-Pb-Ag association (Huston and Large, 1989; Poulsen and Hannington, 1996; Hannington et al., 1999) in which Au is predominantly concentrated in the top of the massive sulfide lens or, here, the up-plunge portion of the 1806 zone. However, it should be emphasized that, mineralogically, Au (electrum) occurs predominantly with Cu (chalcopyrite) throughout the 1806 zone and only with minor sphalerite, predominantly in sulfide stringers and the up-plunge part of the semimassive to massive sulfide lens. Reasons for these contradictory observations (Au-Zn-Pb-Ag association in the up-plunge portion vs. predominant electrum-chalcopyrite assemblage throughout the 1806 zone) are (1) zone refining during the lifespan of the hydrothermal system affecting both the up-plunge and down-plunge portions, (2) late-stage, spatially limited sphalerite bands alternating with galena ± tennantite-tetrahedrite in the upper parts of the up-plunge portion (Figs. 5, 8b), and (3) coeval transport of Cu and Au. The sphalerite bands are interpreted to be formed at declining temperatures during the waning stage of the hydrothermal system creating the Ming deposit because they (1) run mostly parallel to the geologic contacts of the sulfide lens, (2) are weakly sheared (Fig. 5), (3) are restricted to the uppermost parts of the up-plunge portion of the 1806 zone, and (4) show microscopic replacement textures of chalcopyrite by sphalerite and tennantite-tetrahedrite (Fig. 8b).

Ore assemblages and paragenesis: The ore distribution and assemblages in the 1806 zone are complex (Fig. 7), with at least 17 different sulfides, sulfosalts, and precious metal phases present in various amounts in different portions of the ore lens, which has a distinct paragenesis. A premetamorphic paragenetic sequence is presented for the 1806 zone in Figure 13, based on textural relationships between sulfides, sulfosalts, and precious metals, observed metal zoning, and ore mineral chemistry.

Gold-rich VMS deposits (e.g., Boliden, Horne, Bousquet 2, LaRonde Penna, Juan de Fuca Ridge, Lau Basin; Hannington et al., 1986; Large et al., 1989; Tourigny et al., 1989; Huston et al., 1992; Herzig et al., 1993; Herzig and Hannington, 1995; Huston, 2000; Mercier-Langevin et al., 2011, and references therein) are, in general, characterized by relatively complex ore assemblages compared to “precious metal-poor” Cu-Zn-Pb VMS systems. In contrast, orogenic Au deposits have a much simpler sulfide assemblage that consists of variable amounts of one or all of the following minerals: pyrite, chalcopyrite, pyrrhotite, arsenopyrite, and, in rare cases, tennantite-tetrahedrite (e.g., Patey and Wilton, 1993; Evans and Wells, 1998; Groves et al., 1998; Bierlein and Crowe, 2000, and references therein; Ramezani et al., 2000).

The bulk of the Au at the 1806 zone appears to be hosted in mercurian electrum and in minor Ag-Hg-Au alloys (Figs. 8d-i, l-n, 10a, c, d, 12; Table 3; digital Appendix). Native Au, which is very common in orogenic Au deposits (Evans and Wells, 1998; Groves et al., 1998; Bierlein and Crowe, 2000), is not present at the 1806 zone, and invisible Au is almost completely absent, as shown by EPMA analyses of sulfides. Silver at the 1806 zone is intimately associated with the “epithermal suite” of elements (i.e., As, Hg, Sb) in phases such as Ag-bearing tennantite-tetrahedrite, miargyrite, pyrargyrite, and Ag-Hg ± Au alloys (Figs. 8a, g, h, j, k, m, 10g-j, 11e, f, 12; Table 3; digital Appendix). Electrum and Ag phases occur also in close spatial association with minerals containing the epithermal suite of elements, such as arsenopyrite, Ag-bearing tennantite-tetrahedrite, stannite, and boulangerite, usually in the up-plunge part of the 1806 zone (Figs. 8a, d-n, 10). Numerous authors (Sillitoe et al., 1996; Hannington et al., 1999; Huston, 2000; Dubé et al., 2007a) have noted that the occurrence of epithermal suite elements in Au-rich VMS deposits strongly suggests the potential involvement of magmatic fluids or volatiles as the source of precious metal enrichment. This is also assumed for the 1806 zone due to the wide range and occurrence of epithermal suite elements as major and minor components in almost all analyzed minerals and the spatial association between epithermal suite-enriched sulfosalts and precious metals in the up-plunge portion of the 1806 zone. Although high sulfidation assemblages are common to a number of VMS deposits formed in the epithermal environment (Sillitoe et al., 1996, and references therein), the ore assemblage at the 1806 zone is of intermediate sulfidation style, explaining the absence of highly aluminous, acidic alteration assemblages.

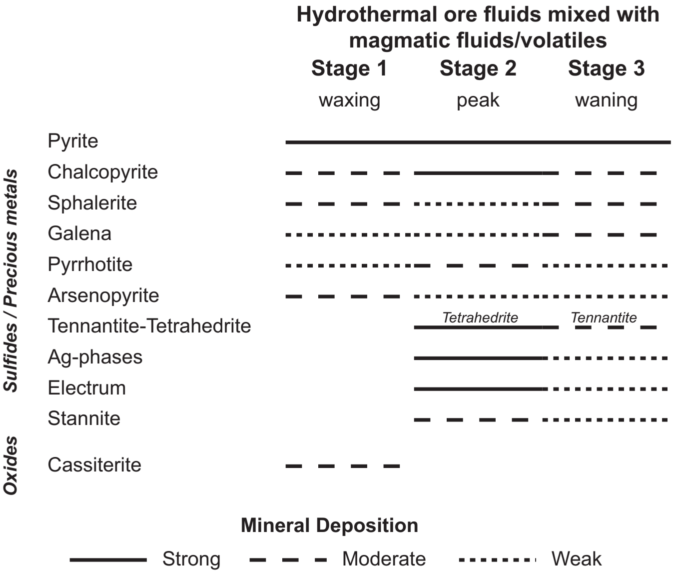

FIG. 13. Paragenetic chart for the syngenetic deposition of sulfides, sulfosalts, precious metals, and cassiterite at the 1806 zone.

Influence of deformation and metamorphism: Despite a predeformation, syngenetic origin for the precious metal enrichment, mineralization and precious metals have been texturally modified during Silurian-Devonian deformation and metamorphism, resulting in local remobilization of precious metals and modifications to mineral textures, especially for pyrite and arsenopyrite. Moreover, in the up-plunge portion of the 1806 zone alloys of AgHg ± Au are often found between recrystallized pyrite and along cracks in recrystallized, brittle deformed pyrite (Fig. 8h), indicating that the occurrence of precious metals with recrystallized and partly brittle deformed pyrite is secondary. Porphyroblasts of pyrite and arsenopyrite are common and, in some cases, contain inclusions of electrum, implying that gold was present prior to porphyroblast formation. Therefore, despite textural modification, the remobilization and recrystallization of gold suggest that it existed prior to metamorphism and deformation and was therefore syngenetic in origin rather than introduced during deformation and metamorphism.

Deposit model for the 1806 zone and hydrothermal ore fluid conditions

A depositional model for the 1806 zone is presented in Figure 14. This model combines the aforementioned evidence from (1) the architecture of the 1806 zone, (2) the alteration assemblage in the rhyolitic footwall, (3) the base metal and precious metal zoning from the down-plunge area to the up-plunge area, and (4) the complex ore assemblages for the syngenetic base and precious metal deposition via seawater and magmatic fluids. Furthermore, the metals, mineral

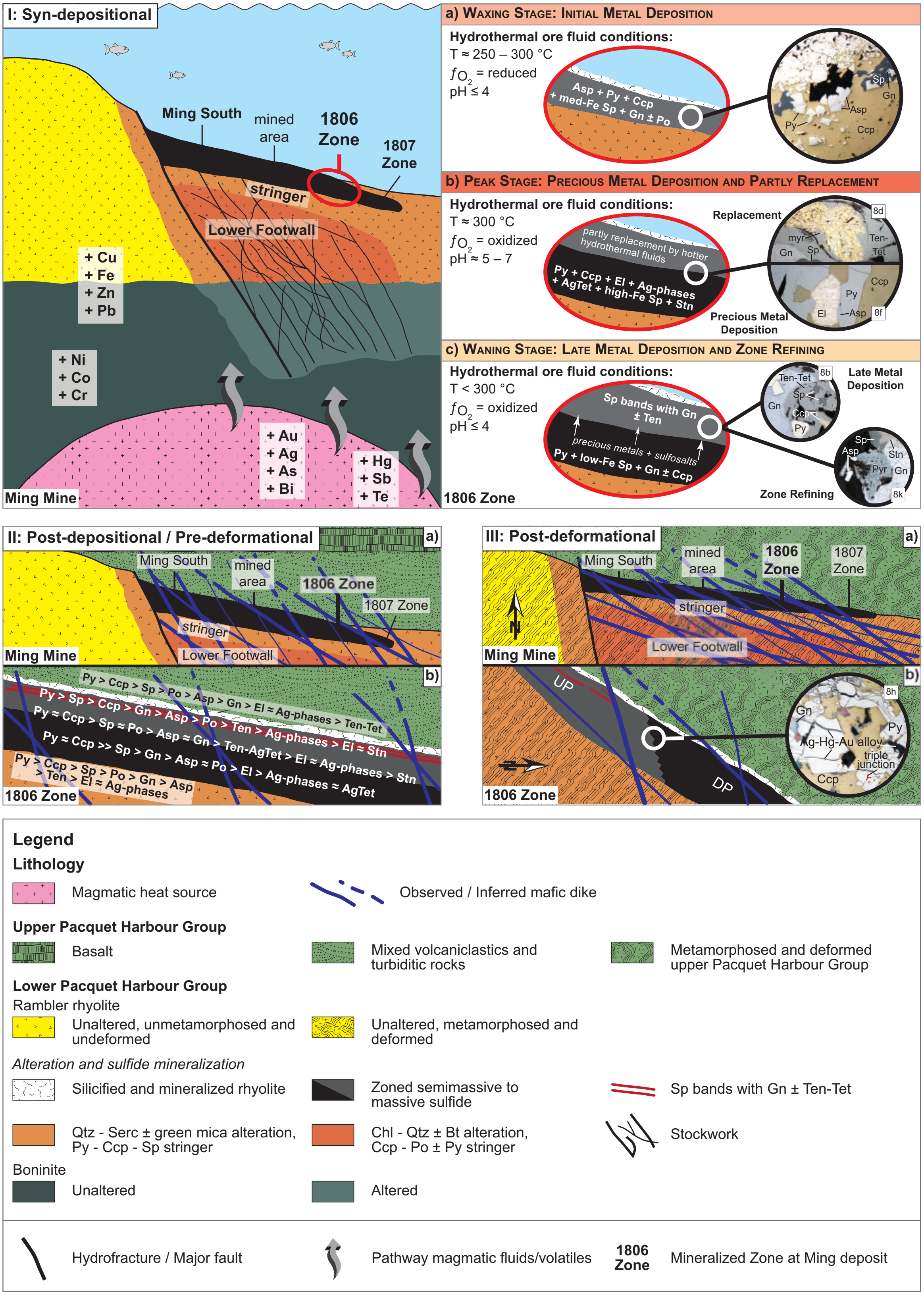

FIG. 14. Depositional model for the genesis of the 1806 zone. (I) Syndepositional processes during waxing (a), peak (b), and waning (c) stages of hydrothermal activity at the 1806 zone. (II) Postdepositional/predeformational state of the Ming deposit (a) and the 1806 zone (b). (III) Postdeformational state of the Ming deposit (a) and the 1806 zone (b); sketches of the 1806 zone in II-b and III-b are perpendicular to II-a and III-a, respectively. Alphanumerical labels in I-b, I-c, and III-b refer to Figures in this paper. See Discussion for details. Mineral abbreviations same as in Figure 8.

assemblages, and paragenesis (Fig. 13) characterizing the 1806 zone provide evidence to constrain the physicochemical fluid conditions (T, pH, f_{O_2}) as the 1806 zone was formed (Fig. 14).

The 1806 zone is part of the broader Ming deposit. Although mafic dikes separate the various sulfide zones (1807 zone, Ming South, Ming North, previously mined area) from each other, it is assumed, given drill core and underground field relationships, that all sulfide lenses once belonged to one continuous lens. The lens has been disrupted by polyphase deformation and metamorphism, resulting in the existing distribution of zones. The 1806 zone is on the edge of the Ming deposit, has the highest Zn grades in the deposit, is associated with abundant epithermal suite element-bearing minerals, and is interpreted to represent the distal portions of a VMS mound (e.g., Lydon, 1988; Ohmoto, 1996; Figs. 3, 14). Given that the deposit has many minerals similar to normal VMS mineralization (e.g., pyrite, sphalerite, chalcopyrite, and galena), but also intermediate sulfidation mineralogy and enrichment in epithermal elements, a hybrid origin is inferred. Support for some component of leaching is consistent with the enrichments in transition metals (Cr, Mn, Ni, and Co) in some sulfides (e.g., sphalerite, arsenopyrite). Additionally, Cr-bearing mica in the alteration mineralization of the silicic footwall is consistent with metal stripping from the wall rock via leaching, because the boninitic footwall to mineralization in the Pacquet Harbour Group is enriched in these elements (Piercey et al., 1997; Skulski et al., 2010). The presence of epithermal mineralogy, however, also requires a magmatic input, likely from some underlying magmatic heat source that has since been sheared off during regional deformation (Fig. 14-I).

During the waxing stage (Fig. 14-Ia) of hydrothermal activity, the up-plunge portion of the 1806 zone with the silicified horizon was formed. In this stage, arsenopyrite-pyrite-chalcopyrite-medium-Fe sphalerite and minor galena-pyrrhotite were deposited by reduced, acidic hydrothermal ore fluids at temperatures of ~250° to 300°C (Heinrich and Eadington, 1986; Lydon, 1988; Large, 1992). Close spatial relations between (partly replaced) arsenopyrite-pyrite-chalcopyrite suggest that the very first hydrothermal ore fluids were strongly reduced, because As is generally transported as an H_3AsO_3 complex that is predominantly dependent on redox conditions (Heinrich and Eadington, 1986).

At the peak of the hydrothermal activity, the down-plunge portion of the 1806 zone was formed and the initial metal assemblage in both the up-plunge portion and the silicified horizon was altered (Fig. 14-Ib). It is suggested that weakly acidic to neutral, oxidized fluids at temperatures of ~300°C caused the deposition of chalcopyrite, Ag-bearing tetrahedrite, and precious metal phases. Evidence for this comes from (1) the predominant occurrence of chalcopyrite with electrum and minor Ag phases and (2) the close chemical and spatial association between Au, Ag, and sulfosalts. Moreover, these hotter, oxidized fluids partly altered the earlier deposited mineral assemblage. This is preserved in (1) myrmekites of replaced arsenopyrite-chalcopyrite-tennantite-tetrahedrite ± electrum ± sphalerite within tennantite-tetrahedrite (Fig. 8c, d) and (2) chalcopyrite disease in sphalerites. Besides pyrite, chalcopyrite, precious metals, and sulfosalts, minor high-Fe sphalerites were deposited, since they are abundant throughout the 1806 zone and in silicified footwall rhyolite. Chalcopyrite disease is present in the high-Fe sphalerites as well, but it is less abundant than in medium-Fe sphalerites. It is assumed that gold was transported as a chlorocomplex during this phase, given the strong association with chalcopyrite and assumed temperatures greater than 300°C (e.g., Seward, 1973; Hannington and Scott, 1989b; Huston and Large, 1989; Large et al., 1989; Stefánsson and Seward, 2004; Williams-Jones et al., 2009).

The waning stage of hydrothermal activity is characterized by (1) deposition of sphalerite-galena and minor tennantite within sphalerite bands within the up-plunge portion of the 1806 zone and (2) zone refining affecting especially precious metals and sulfosalts (Fig. 14-Ic). Within the sphalerite bands, chalcopyrite is often replaced by sphalerite and tennantite-tetrahedrite (Fig. 8b). Moreover, the elevated grades of Au and Ag (Fig. 9) and the higher abundance of precious metals (Fig. 7) in the up-plunge area are a direct result of zone refining during this stage, since the vast majority of the precious metals were originally deposited at peak hydrothermal activity. Lower-temperature (<300°C), nearly oxidized and reduced fluids transported mainly Zn and Pb (Seward, 1984; Lydon, 1988; Large, 1992; Reed and Palandri, 2006) at the waning stage of hydrothermal activity. However, the same fluids are also responsible for the remobilization of Au, Ag, and epithermal suite elements (As, Sb; Seward, 1976; Zotov et al., 2003; Reed and Palandri, 2006). At the waning stage, Au was finally remobilized from the down-plunge portion by lower-temperature, Zn-Pb-Ag-Sb–bearing fluids, likely as a bisulfide complex (e.g., Seward, 1973; Huston and Large, 1989; Large et al., 1989; Williams-Jones et al., 2009) with Ag and epithermal suite elements, and deposited in the up-plunge part, usually with Ag phases and sulfosalts.

The postdepositional, predeformational state of the 1806 zone is illustrated in Figure 14-II. A vertical metal zoning within the massive sulfide horizon is clearly developed with a pyrite-chalcopyrite assemblage at the bottom (now the down-plunge portion) and a pyrite-chalcopyrite-sphalerite assemblage with local sphalerite bands on top (now the up-plunge portion). Mafic dikes intruded syn- and postdepositionally and crosscut the Ming deposit with the 1806 zone (Pilote and Piercey, 2013).

During Silurian-Devonian metamorphism and deformation, the shape of the Ming deposit in general and of the 1806 zone in particular was deformed (Fig. 14-III; Table 1), resulting in the elongation of the sulfide lenses parallel to a regional F2 foliation (Castonguay et al., 2009). It is also assumed that the sulfide horizon at the 1806 zone was internally sheared, resulting in (1) the flattening and elongation of the sulfide lens, (2) the reorientation of the original, almost horizontal metal zoning to the recent metal zoning observed in the up-plunge and down-plunge portions, and (3) recrystallization of minerals within the ores.

The results presented herein support that the 1806 zone of the Ming mine formed as a result of zone refining, leaching, and magmatic-hydrothermal input into a seafloor hydrothermal system. Despite deformation and metamorphism, these processes have not introduced new gold into the deposit but only remobilized existing syngenetic precious metals.

Conclusion

The results from stratigraphy, alteration, metal distribution, ore assemblage, and mineral chemistry presented in this paper show the following:

1. Precious metal emplacement in the metamorphosed and (polyphase) deformed Au-bearing Ming VMS deposit is likely syngenetic despite the lack of advanced argillic alteration. An intermediate sulfidation style of mineralization, as well as normal VMS formation, is responsible for the sericitic alteration observed in the rhyolitic footwall and is rather typical of low sulfidation epithermal deposits and base metal VMS deposits.
2. The deposition of precious metals occurred coeval with base metal sulfides, especially chalcopyrite. However, mineral chemistry strongly supports the involvement of magmatic-hydrothermal fluids containing precious metals and epithermal suite elements to normal VMS hydrothermal fluids containing base and transition metals.
3. Metamorphism and polyphase deformation changed the deposit architecture and massive sulfide geometry in the sense that the mineralized zones at the Ming deposit are now separated by mafic dikes and the original vertical metal zoning is now sheared as seen from the different metal associations in the up-plunge (Cu-Zn-Au-Ag) and down-plunge (Cu-Au) portions. Moreover, the massive sulfide lenses are elongated parallel to foliation. Mineral textures were also altered, as seen in the recrystallization of many sulfide phases and the partial syndeformational remobilization of precious metals (occurrence along cracks and grain boundaries of recrystallized pyrite). However, deformation and metamorphism have only modified existing precious distributions and have not resulted in synorogenic gold additions similar to orogenic Au deposits (Deer Cove, Stog'er Tight) found regionally on the Baie Verte Peninsula.

Acknowledgments

Michael Shaffer and David Grant (Bruneau Centre, MUN) are thanked for their great support and help in the use of the SEM and its software. SMB thanks Yanan Liu (UT) for her assistance and help at the EPMA at UT. An SEG Student Research Grant to SMB was partly used for analytical work at the EPMA at UT. Discussions with Sean McClenaghan, Patrick Mercier-Langevin, and George Hudak improved the paper in the early stages of the manuscript. Special thanks go to Scott Swinden, Patrick Mercier-Langevin, and David Lentz, who improved the paper significantly with their critical and constructive reviews and comments. Staff and miners of the Ming mine are thanked for their help, assistance, and support during core logging and underground mapping. Rambler Metals and Mining Canada Ltd. provided logistical support for the project. Funding for the project was provided by grants to S.J. Piercey, including an NSERC Discovery Grant and the NSERC Altius Industrial Research Chair in Mineral Deposits supported by NSERC, Altius Minerals Ltd., and the Research and Development Corporation of Newfoundland and Labrador.

REFERENCES

Bergman-Weihed, J., Bergström, U., Billström, K., and Weihed, P., 1996, Geology, tectonic setting, and origin of the Paleoproterozoic Boliden Au-Cu-As deposit, Skellefte district, northern Sweden: ECONOMIC GEOLOGY, v. 91, p. 1073–1097.

Bierlein, F.P., and Crowe, D.E., 2000, Phanerozoic orogenic lode gold deposits, *in* Hagemann, S.G., Brown, P.E., ed., Gold in 2000, 13. Reviews in Economic Geology: Boulder, CO, Society of Economic Geologists, p. 103–139.

Brueckner, S.M., Piercey, S.J., Sylvester, P.J., Pilgrim, L., Maloney, S., Hyde, D., and Ogilvie, G., 2011, Stratigraphy, mineralogy, geochemistry, and genesis of an Au-rich volcanogenic massive sulfide (VMS) system from the Baie Verte Peninsula, NW Newfoundland, Canada: The 1806 zone as an example from the Ming mine, Rambler Camp, *in* Deschênes, G., Dimitrakopoulos, R., and Bouchard, J., eds., World Gold 2011: Montreal, QC, Canada, Canadian Institute of Mining, Metallurgy and Petroleum, p. 899–911.

Castonguay, S., Skulski, T., van Staal, C., and Currie, M., 2009, New insights on the structural geology of the Pacquet Harbour Group and Point Rousse Complex, Baie Verte Peninsula, Newfoundland: Newfoundland and Labrador Department of Natural Resources, Geological Survey, Current Research, Report 09-1, p. 147–158.

Cawood, P.A., van Gool, J.A.M., and Dunning, G.R., 1993, Silurian age for movement on the Baie Verte Line: Implications for accretionary tectonics in the northern Appalachians: Geological Society of America, Abstract with Programs, v. 25, A422.

Di Benedetto, F., Bernardini, G.P., Costagliola, P., Plant, D., and Vaughan, D.J., 2005, Compositional zoning in sphalerite crystals: American Mineralogist, v. 90, p. 1384–1392.

Dubé, B., Gosselin, P., Mercier-Langevin, P., Hannington, M., and Galley, A., 2007a, Gold-rich volcanogenic massive sulphide deposits: Geological Association of Canada, Mineral Deposits Division, Special Publication no. 5, p. 75-94.

Dubé, B., Mercier-Langevin, P., Hannington, M., Lafrance, B., Gosselin, G., and Gosselin, P., 2007b, The LaRonde Penna world-class Au-rich volcanogenic massive sulfide deposit, Abitibi, Québec: Mineralogy and geochemistry of alteration and implications for genesis and exploration: ECONOMIC GEOLOGY, v. 102, p. 633–666.

Evans, D.T.W., and Wells, C., 1998, Epigenetic gold mineralization, Baie Verte Peninsula, Newfoundland: Newfoundland Department of Mines and Energy, Geological Survey, Current Research, Report 98-1, p. 39–51.

Franklin, J.M., 1993, Volcanic-associated massive sulphide deposits: Geological Association of Canada, Special Paper 40, p. 315–334.

——1996, Volcanic-associated massive sulphide base metals: Ottawa, ON, Geological Survey of Canada, Geology of Canada Series, no. 8, p. 158–183.

Franklin, J.M., Lydon, J.W., and Sangster, D.F., 1981, Volcanic-associated sulfide deposits: ECONOMIC GEOLOGY 75TH ANNIVERSARY VOLUME, p. 485–627.

Franklin, J.M., Gibson, H.L., Jonasson, I.R., and Galley, A.G., 2005, Volcanogenic massive sulfide deposits: ECONOMIC GEOLOGY 100TH ANNIVERSARY VOLUME, p. 523–560.

Galley, A., Hannington, M., and Jonasson, I., 2007, Volcanogenic massive sulphide deposits: Geological Association of Canada, Mineral Deposits Division, Special Publication no. 5, p. 141–161.

Goldfarb, R.J., Baker, T., Dubé, B., Groves, D.I., Hart, C.J.R., and Gosselin, P., 2005, Distribution, character, and genesis of gold deposits in metamorphic terranes: ECONOMIC GEOLOGY 100TH ANNIVERSARY VOLUME, p. 407–450.

Groves, D.I., Goldfarb, R.J., Gebre-Mariam, M., Hagemann, S.G., and Robert, F., 1998, Orogenic gold deposits: A proposed classification in the context of their crustal distribution and relationship to other gold deposit types: Ore Geology Reviews, v. 13, p. 7–27.

Hannington, M.D., and Scott, S.D., 1989a, Gold mineralization in volcanogenic massive sulfides: Implications of data from active hydrothermal vents on the modern seafloor: Economic Geology Monograph 6, p. 491–507.

——1989b, Sulfidation equilibria as guides to gold mineralization in volcanogenic massive sulfides: Evidence from sulfide mineralogy and the composition of sphalerite: ECONOMIC GEOLOGY, v. 84, p. 1978–1995.

Hannington, M.D., Peter, J.M., and Scott, S.D., 1986, Gold in sea-floor polymetallic sulfide deposits: ECONOMIC GEOLOGY, v. 81, p. 1867–1883.

Hannington, M.D., Poulsen, K.H., Thompson, J.F.H., and Sillitoe, R.H., 1999, Volcanogenic gold in the massive sulfide environment: Reviews in Economic Geology, v. 8, p. 325–351.

Hedenquist, J.W., Arribas, R.A., and Gonzalez-Urien, E., 2000, Exploration for epithermal gold deposits: Reviews in Economic Geology, v. 13, p. 245–277.

Heinrich, C.A., and Eadington, P.J., 1986, Thermodynamic predictions of the hydrothermal chemistry of arsenic, and their significance for the paragenetic sequence of some cassiterite-arsenopyrite-base metal sulfide deposits: ECONOMIC GEOLOGY, v. 81, p. 511–529.

Herzig, P.M., and Hannington, M.D., 1995, Polymetallic massive sulfides at the modem seafloor: A review: Ore Geology Reviews, v. 10, p. 95–115.

Herzig, P.M., Hannington, M.D., Fouquet, Y., von Stackelberg, U., and Petersen, S., 1993, Gold-rich polymetallic sulfides from the Lau back arc and implications for the geochemistry of gold in sea-floor hydrothermal systems of the southwest Pacific: Economic Geology, v. 88, p. 2182–2209.

Hibbard, L.J., 1983, Geology of the Baie Verte Peninsula, Newfoundland: Department of Mines and Energy, Government of Newfoundland and Labrador, Memoir 2, 279 p.

Huston, D.L., 2000, Gold in volcanic-hosted massive sulfide deposits: Distribution, genesis, and exploration: Reviews in Economic Geology, v. 13, p. 401–426.

Huston, D.L., and Large, R.R., 1989, A chemical model for the concentration of gold in volcanogenic massive sulphide deposits: Ore Geology Reviews, v. 4, p. 171–200.

Huston, D.L., Bottril, R.S., Creelman, R.A., Zaw, K., Ramsden, T.R., Rand, S.W., Gemmell, J.B., Jablonski, W., Sie, S.H., and Large, R.R., 1992, Geologic and geochemical controls on the mineralogy and grain size of gold-bearing phases, eastern Australian volcanic-hosted massive sulfide deposits: Economic Geology, v. 87, p. 542–563.

Large, R.R., 1977, Chemical evolution and zonation of massive sulfide deposits in volcanic terrains: Economic Geology, v. 72, p. 549–572.

——1992, Australian volcanic-hosted massive sulfide deposits: Features, styles, and genetic models: Economic Geology, v. 87, p. 471–510.

Large, R.R., Huston, D.L., McGoldrick, P.J., and Ruxton, P.A., 1989, Gold distribution and genesis in Australian volcanogenic massive sulfide deposits and their significance for gold transport models: Economic Geology Monograph 6, p. 520–536.

Lydon, J.W., 1984, Volcanogenic massive sulphide deposits. Part 1: A descriptive model: Geoscience Canada, v. 11, p. 195–202.

——1988, Volcanogenic massive sulphide deposits. Part 2: Genetic models: Geoscience Canada, v. 15, p. 43–65.

Marquis, P., Hubert, C., Brown, A.C., and Rigg, D.M., 1990, Overprining of early, redistributed Fe and Pb-Zn mineralization by late stage Au-Ag-Cu deposition at the Dumagami mine, Bousquet district, Abitibi, Quebec: Canadian Journal of Earth Sciences, v. 27, p. 1651–1671.

Mercier-Langevin, P., Hannington, M.D., Dubé, B., and Bécu, V., 2011, The gold content of volcanogenic massive sulfide deposits: Mineralium Deposita, v. 46, p. 509–539.

Mercier-Langevin, P., McNicoll, V., Allen, R.L., Blight, J.H.S., and Dubé, B., 2013, The Boliden gold-rich volcanogenic massive sulphide deposit, Skellefte district, Sweden: New U-Pb age constraints and implications at deposit and district scale: Mineralium Deposita, v. 48, p. 485–504.

Moëlo, Y., Makovicky, E., Mozgova, N.N., Jambor, J.L., Cook, N., Pring, A., Paar, W., Nickel, E.H., Graesser, S., Karup-Møller, S., Balic-Zunic, T., Mumme, W.G., Vurro, F., Topa, D., Bindi, L., Bente, K., and Shimizu, M., 2008, Sulfosalt systematics: A review. Report of the sulfosalt sub-committee of the IMA Commission on Ore Mineralogy: European Journal of Mineralogy, v. 20, p. 7–46.

Ohmoto, H., 1996, Formation of volcanogenic massive sulfide deposits: The Kuroko perspective: Ore Geology Reviews, v. 10, p. 135–177.

Patey, K.S., and Wilton, D.H.C., 1993, The Deer Cove deposit, Baie Verte Peninsula, Newfoundland, a Paleozoic mesothermal lode-gold occurrence in the northern Appalachians: Canadian Journal of Earth Sciences, v. 30, p. 1532–1546.

Piercey, S., Jenner, G.A., and Wilton, D.H.C., 1997, The stratigraphy and geochemistry of the southern Pacquet Harbour Group, Baie Verte Peninsula, Newfoundland: Implications for mineral exploration: Current Research Newfoundland and Labrador Department of Natural Resources, Geological Survey, Report 97-1, p. 119–139.

Pilgrim, L., 2009, Mineral resource estimate for the Ming mine, Newfoundland, Canada: Baie Verte, NL, Rambler Metals and Mining Canada Ltd, Form 43-101F, Technical Report, p. 114.

Pilote, J.-L., and Piercey, S.J., 2013, Volcano-stratigraphy of the 1807 zone of the Ming Cu-Au volcanogenic massive sulfide (VMS) deposit, Baie Verte Peninsula, northern Newfoundland: Ottawa, ON, Geological Survey of Canada, Current Research, 2013-20, 13 p.

Poulsen, K.H., and Hannington, M.D., 1996, Volcanic-associated massive sulphide gold: Ottawa, ON, Geological Survey of Canada, Geology of Canada Series, no. 8, p. 183–196.

Poulsen, K.H., Robert, F., and Dubé, B., 2000, Geological classification of Canadian gold deposits: Ottawa, ON, Geological Survey of Canada, 113 p.

Ramezani, J., Dunning, G.R., and Wilson, M.R., 2000, Geologic setting, geochemistry of alteration, and U-Pb age of hydrothermal zircon from the Silurian Stog'er Tight gold prospect, Newfoundland Appalachians, Canada: Exploration and Mining Geology, v. 9, p. 171–188.

Reed, M.H., and Palandri, J., 2006, Sulfide mineral precipitation from hydrothermal fluids: Reviews in Mineralogy and Geochemistry, v. 61, p. 609–631.

Roth, T., Thompson, J.F.H., and Sillitoe, R.H., 1999, The precious metal-rich Eskay Creek deposit, northwestern British Columbia: Reviews in Economic Geology, v. 8, p. 357–373.

Seward, T.M., 1973, Thio complexes of gold and the transport of gold in hydrothermal ore solutions: Geochimica et Cosmochimica Acta, v. 37, p. 379–399.

——1976, The stability of chloride complexes of silver in hydrothermal solutions up to 350°C: Geochimica et Cosmochimica Acta, v. 40, p. 1329–1341.

——1984, The formation of lead(II) chloride complexes to 300°C: A spectrophotometric study: Geochimica et Cosmochimica Acta, v. 48, p. 121–134.

Sillitoe, R.H., and Hedenquist, J.W., 2003, Linkages between volcanotectonic settings, ore-fluid compositions, and epithermal precious metal deposits: Society of Economic Geologists Special Publication no. 10, p. 315–343.

Sillitoe, R.H., Hannington, M.D., and Thompson, J.F.H., 1996, High sulfidation deposits in the volcanogenic massive sulfide environment: Economic Geology, v. 91, p. 204–212.

Skulski, T., Castonguay, S., van Staal, C., Rogers, N., McNicoll, V., Kerr, A., and Escayola, M., 2009, Baie Verte Peninsula: An evolving geological story, *in* Rogers, N., and Kerr, A., eds., Annual Field Trip, October 2–5, 2009: St. John's, NL, Geological Association of Canada, Newfoundland and Labrador Section, p. 76.

Skulski, T., Castonguay, S., McNicoll, V., van Staal, C., Kidd, W., Rogers, N., Morris, W., Ugalde, H., Slavinski, H., Spicer, W., Moussallam, Y., and Kerr, I., 2010, Tectonostratigraphy of the Baie Verte oceanic tract and its ophiolite cover sequence on the Baie Verte Peninsula: Newfoundland and Labrador Department of Natural Resources, Geological Survey, Current Research, Report 10-1, p. 315–335.

Stefánsson, A., and Seward, T.M., 2004, Gold(I) complexing in aqueous sulphide solutions to 500°C at 500 bar: Geochimica et Cosmochimica Acta, v. 68, p. 4121–4143.

Swinden, H.S., and Thorpe, R.I., 1984, Variations in style of volcanism and massive sulfide deposition in Early to Middle Ordovician island-arc sequences of the Newfoundland Central mobile belt: Economic Geology, v. 79, p. 1596–1619.

Tourigny, G., Brown, A.C., Hubert, C., and Crépeau, R., 1989, Syvolcanic and syntectonic gold mineralization at the Bousquet mine, Abitibi greenstone belt, Quebec: Economic Geology, v. 84, p. 1875–1890.

Tourigny, G., Doucet, D., and Bourget, A., 1993, Geology of the Bousquet 2: An example of a deformed, gold-bearing, polymetallic sulfide deposit: Economic Geology, v. 88, p. 1578–1597.

Tuach, J., 1988, Geology and sulphide mineralization in the Pacquet Harbour Group, *in* Swinden, H.S., and Kean, B.F., eds., The volcanogenic sulphide districts of central Newfoundland: A guidebook and reference manual for volcanogenic sulphide deposits in the early Paleozoic oceanc volcanic terranes of central Newfoundland: St. John's, NL, Geological Association of Canada, Mineral Deposits Division, p. 49–53.

Tuach, J., and Kennedy, M.J., 1978, The geologic setting of the Ming and other sulfide deposits, consolidated Rambler mines, northeast Newfoundland: Economic Geology, v. 73, p. 192–206.

van Staal, C.R., 2007, Pre-Carboniferous tectonic evolution and metallogeny of the Canadian Appalachians: Geological Association of Canada, Mineral Deposits Division, Special Publication no. 5, p. 793–818.

van Staal, C.R., and Barr, S.M., 2012, Lithosperic architecture and tectonic evolution of the Canadian Appalachians and associated Atlantic margin: Geological Association of Canada, Special Paper 49, p. 41–96.

Vaughan, D.J., and Craig, J.R., 1978, Mineral chemistry of metal sulfides: Cambridge, Cambridge University Press, 493 p.

Wagner, T., and Jonsson, E., 2001, Mineralogy of sulfosalt-rich vein-type ores, Boliden massive sulfide deposit, Skellefte district, northern Sweden: The Canadian Mineralogist, v. 39, p. 855–872.

Williams, H., 1979, Appalachian orogen in Canada: Canadian Journal of Earth Sciences, v. 16, p. 792–807.

Williams-Jones, A.E., Bowell, R.J., and Migdisov, A.A., 2009, Gold in solution: Elements, v. 5, p. 281–287.

Wright, K., 2009, The incorporation of cadmium, manganese and ferrous iron in sphalerite: Insights from computer simulations: The Canadian Mineralogist, v. 47, p. 615–623.

Zotov, A.V., Shikina, N.D., and Akinfiev, N.N., 2003, Thermodynamic properties of the Sb(III) hydroxide complex $Sb(OH)_3(aq)$ at hydrothermal conditions: Geochimica et Cosmochimica Acta, v. 67, p. 1821–1836.